JEM Journal of Experimental Medicine

ARTICLE

Mechanosensing through YAP controls T cell activation and metabolism

Kevin P. Meng[1], Fatemeh S. Majedi[2], Timothy J. Thauland[3], and Manish J. Butte[3,4]

Upon immunogenic challenge, lymph nodes become mechanically stiff as immune cells activate and proliferate within their encapsulated environments, and with resolution, they reestablish a soft baseline state. Here we show that sensing these mechanical changes in the microenvironment requires the mechanosensor YAP. YAP is induced upon activation and suppresses metabolic reprogramming of effector T cells. Unlike in other cell types in which YAP promotes proliferation, YAP in T cells suppresses proliferation in a stiffness-dependent manner by directly restricting the translocation of NFAT1 into the nucleus. YAP slows T cell responses in systemic viral infections and retards effector T cells in autoimmune diabetes. Our work reveals a paradigm whereby tissue mechanics fine-tune adaptive immune responses in health and disease.

Introduction

At the molecular scale, mechanical forces are required for the activation of integrins and for signaling through the TCR (Liu et al., 2014; Kim et al., 2009; Hu and Butte, 2016). Proximal signaling of the TCR is potentiated when peptide-MHC or antibody to CD3 is anchored to stiff matrices, stiff polymer pillars, or stiff APCs (Roy and Burkhardt, 2018; Saitakis et al., 2017; Liu et al., 2016; Judokusumo et al., 2012). Integrins such as LFA-1 on T cells are also sensitive to molecular scale mechanical forces, which promote increased adhesion between T cells and APCs (Comrie et al., 2015; Li et al., 2016; Alon and Dustin, 2007). However, T cells also encounter a variety of forces at the tissue scale as they travel through diverse microenvironments, including sites of infection, inflammation, and autoimmunity. Mechanosensation of the tissue microenvironment can be mediated by a variety of receptors or directly by the cytoskeleton (Discher et al., 2005). Yes-associated protein (YAP) is the best known sensor of microenvironmental mechanics and is dominantly regulated by the stiffness of the extracellular matrix (Dupont et al., 2011). Understanding microenvironmental mechanosensing has proven revolutionary in the fields of cellular development, organ size regulation, stem cell differentiation, cancer metastasis, cellular senescence, and programmed cell death (Dong et al., 2007; Lian et al., 2010; Lamar et al., 2012; Zhao et al., 2008). Recent works have established a role for YAP in immunity, but there have been no links yet between YAP and tissue mechanics in immune cells (Fan et al., 2017; Ni et al., 2018; Wang et al., 2017; Thaventhiran et al., 2012). Furthermore, environmental mechanosensing has not been demonstrated in T cells.

The metabolic state of T cells is central to the adaptive immune response. Quiescent T cells have low metabolic activity, but they undergo considerable reprogramming upon activation, up-regulating glycolysis and glutaminolysis to provide energy and the building blocks for cellular proliferation. Regulation of many of these metabolic changes has largely been ascribed to transcription driven by NFAT (Mak et al., 2017; Klein-Hessling et al., 2017; Vaeth et al., 2017). Thus, factors that influence NFAT activation are expected to influence T cell metabolism, as is seen, for example, in genetic loss of *STIM1* or *ORAI1* in mice and humans (Lian et al., 2017). Moreover, NFAT does not serve as a binary switch, but rather offers fine-tuned and dynamic regulation of a variety of genes. Indeed, regulation of NFAT1 activation and trafficking from the cytoplasm to the nucleus involve over a dozen proteins, many of which interact with IQGAP1, a cytoplasmic scaffold protein (Gorman et al., 2012). A variety of inputs converging on IQGAP1 and its partners allows for nuanced regulation of NFAT, which permits fine-tuning of immune responses. In clinical practice, the central role of NFAT allows for important modulation of many T cell effector responses by the NFAT-modulating drugs cyclosporine A or tacrolimus in autoimmunity, allotransplantation, and graft-versus-host disease (Ekberg et al., 2007).

To understand the impact of forces at the tissue scale, we studied LN mechanics during infection. Activated LNs become

[1]Department of Microbiology and Immunology, Stanford University, Stanford, CA; [2]Department of Bioengineering, University of California, Los Angeles, Los Angeles, CA; [3]Division of Immunology, Allergy, and Rheumatology, Department of Pediatrics, University of California, Los Angeles, Los Angeles, CA; [4]Department of Microbiology, Immunology, and Molecular Genetics, University of California, Los Angeles, Los Angeles, CA.

Correspondence to Manish J. Butte: Mbutte@ucla.edu.

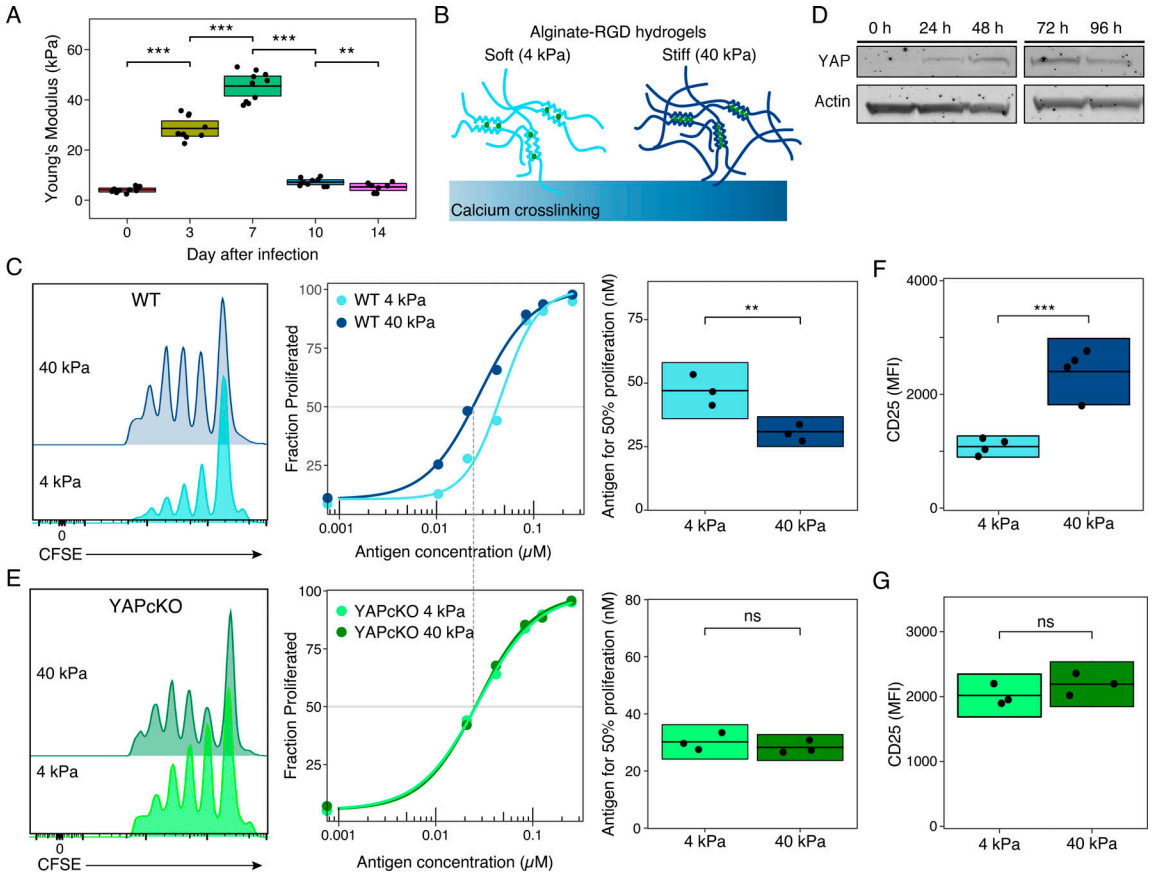

Figure 1. **Tissue mechanics regulate T cell proliferation and activation. (A)** Inguinal and brachial LNs from mice infected with LCMV Armstrong were measured for mechanical stiffness. Each point represents one LN. Two or three LNs were measured from each mouse with three mice at each time point. Data representative of three independent experiments. Box shows mean and 95% CI. **(B)** Schematic of 4 kPa (soft) and 40 kPa (stiff) scaffolds generated by alginate-RGD cross-linked with calcium. **(C and E)** Left: Proliferation of CFSE-labeled SMARTA (C) WT or (E) YAPcKO T cells cultured with WT mitomycin-C–treated splenocytes and 42 nM GP_{61-80} peptide on soft or stiff 2D scaffolds. Center: Proliferation responses to multiple antigen doses led to calculation of ED_{50} from three independent dose–response experiments (right). Each dot is an independent experiment. Box shows mean and 95% CI. **(D)** Immunoblot for YAP at different time points in stimulated mouse $CD4^+$ T cells. Data representative of three independent experiments. **(F and G)** CD25 expression after 24 h of SMARTA (F) WT or (G) YAPcKO T cells cultured with WT splenocytes and peptide on soft or stiff 2D scaffolds. Each dot is an independent experiment. Box shows mean and 95% CI. Permutation P values: *, $P < 0.05$; **, $P < 0.01$; ***, $P < 0.001$. MFI, mean fluorescence intensity; ns, not significant.

stiff and swollen during an immune response, but shrink and return to a baseline of mechanical softness upon resolution. Thus, the rise and fall of the adaptive immune response appears to synchronize with changes in LN stiffness. To shed light on T cell pathophysiology in disease-associated tissues, we sought to determine how mechanical signals translate to regulation of the T cell effector program.

Results

Tissue mechanics regulate T cell proliferation and activation

Infections have been noted for centuries to cause inflammation and induce rigidity of regional LNs. To quantitate the physiological changes in LN stiffness over the course of an infection, we measured the bulk stiffness of LNs of mice acutely infected with lymphocytic choriomeningitis virus (LCMV). We observed an ~10-fold increase of stiffness (elastic modulus) at days 3 and 7, followed by a return to baseline by day 10 (Fig. 1 A). The size of the LN, which is driven by lymphoproliferation, roughly matched these mechanical changes (Fig. S1 A).

We sought to understand how the varying mechanical cues experienced by T cells during an immune response affect their activation and function. However, many properties of the LN microenvironment change during a viral infection in addition to stiffness, e.g., inflammatory cytokines, activated dendritic cells and their costimulatory potential, fibroblastic reticular cells and their chemokine expression, and more. These considerations led us to generate biomimetic alginate-RGD (Arg-Gly-Asp peptide) scaffolds with elastic moduli of 4 kPa (soft) and 40 kPa (stiff) that recapitulated the LN mechanics observed in vivo (Fig. 1 B and Fig. S1, B–E). Alginate scaffolds also demonstrated similar stress relaxation kinetics to tissue, unlike polymers used in previous studies (Judokusumo et al., 2012; Fig. S1 F). To focus on the mechanical environment and eliminate the impact of the scaffold itself presenting antigenic signals, we co-cultured peptide-loaded syngeneic splenocytes with SMARTA TCR transgenic $CD4^+$ T cells atop these scaffolds for 2–4 d. T cells

cultured on the softer substrate required approximately twofold more peptide to achieve 50% of maximal proliferation (ED_{50}; Fig. 1 C). Activating T cells with peptide-loaded APCs in the context of softer surfaces also led to reduced expression of activation markers including CD25 (Fig. 1 F).

The mechanosensor YAP plays an important role in the growth and differentiation of varied cell types. To test whether YAP is expressed in $CD4^+$ T cells, we measured expression in T cells from WT mice ex vivo and after stimulation. We discovered that YAP is induced upon T cell activation on both the transcriptional (Fig. S1 G) and protein level (Fig. 1 D). We observed increased nuclear localization of YAP in activated T cells cultured on stiff hydrogels (Fig. S1 H). Thus, YAP is expressed and responds to the mechanical microenvironment in activated T cells. To determine if YAP plays a role in mechanosensing in T cells, we created a conditional KO of YAP (YAPcKO) by crossing YAP flox mice to CD4-cre mice. YAP protein was absent in both $CD4^+$ and $CD8^+$ effector T cells from these mice (Fig. S1 I). We did not observe any developmental defects in thymic, splenic, or LN T cells in YAPcKO mice (Fig. S2, A–D). Furthermore, we found no difference in percentages of natural $Foxp3^+$ regulatory T cells (T reg cells; Fig. S2 E), and normal induction of induced T reg cells and Th17 cells (Fig. S2, E and F).

To test whether the differences in T cell responses we observed on stiff and soft hydrogels were YAP dependent, we conducted the same experiments with SMARTA YAPcKO T cells. We found that YAPcKO T cells demonstrated equivalent proliferation when cultured on stiff and soft substrates, comparable to the level of WT cells cultured atop stiff substrates (Fig. 1 E; see dashed line connecting Fig. 1 C and Fig. 1 E). The activation marker CD25 was equivalently up-regulated in YAPcKO T cells in stiff and soft environments as well (Fig. 1 G). Thus, YAP is necessary for T cells to differentially respond to their mechanical microenvironment.

To investigate the transcriptional response of T cells to the mechanical microenvironment, we performed RNA sequencing (RNA-seq) of WT and YAPcKO effector T cells cultured on soft or stiff scaffolds. In WT T cells, high stiffness led to an up-regulation of 169 genes and down-regulation of 293 genes (Fig. S2 G). Loss of YAP led to abrogation of a large majority of those differentially regulated genes, suggesting that YAP is a major regulator of mechanosensing in T cells (Fig. S2 H). Differentially expressed genes in WT T cells in the stiff and soft states were examined by principal component analysis. WT T cells experiencing a soft microenvironment were separated from WT T cells experiencing a stiff microenvironment by principal component 2 (Fig. S2 I). These results show that YAP is needed for most of the differential transcriptional and effector responses of T cells activated in mechanically stiff versus soft microenvironments.

YAP restricts TCR-induced $CD4^+$ T cell activation and proliferation

We sought to understand if YAP influenced the early activation of T cells or downstream effector responses. YAPcKO $CD4^+$ T cells proliferated more than WT T cells, with a decrease in the ED_{50} of anti-CD3 of 1.5-fold (Fig. 2 A). Activated YAPcKO T cells also secreted more IL-2 (Fig. 2 B) and showed a marked increase in activation markers, including CD69, CD25, and CD44 (Fig. 2 C). Thus, YAP inhibits effector responses. When mechanical forces are applied through the TCR complex, there are alterations in proximal signaling (Judokusumo et al., 2012; Bashour et al., 2014). However, acutely stimulated WT or YAPcKO T cells showed no differences in phospho-tyrosine bands at 76 kD (SLP-76) and 38 kD (linker for activation of T cells [LAT]; Fig. S2 J). Thus, YAP does not affect early activation of T cells, which suggests that the YAP-dependent proliferative effects are unrelated to mechanosensation by the TCR.

To confirm that YAP negatively regulates T cell proliferation and activation, we performed a rescue experiment. OT-II TCR transgenic YAPcKO T cells were transduced with full-length WT-YAP (WT-YAP) or a control vector, then restimulated. YAP expression decreased proliferation, IL-2 production, and CD25 expression compared with control (Fig. 2, D–F). Taken together, these data establish YAP as a suppressor of T cell effector responses. This result also shows that two different TCR transgenics show similar results.

YAP inhibits antiviral T cell effector response

YAP has been implicated in the innate immune response to viral infection (Wang et al., 2017). Thus, we wondered whether YAP influenced adaptive immunity in viral infections. We cotransferred equal numbers of congenic, naive WT and YAPcKO SMARTA T cells and then infected recipients with LCMV (Fig. 3 A). YAPcKO SMARTA T cells held a significant proliferative advantage (Fig. 3 B), and had heightened expression of activation markers and cytokines (Fig. 3 C). These results show a cell-intrinsic effect of YAP on suppressing T cell effector responses to a viral infection.

To test whether YAP expression could rescue the observed phenotype, we transduced WT-YAP or a control vector into YAPcKO SMARTA T cells and cotransferred them into CD45.1 mice infected with LCMV (Fig. 3 D). Consistent with our in vitro data, expression of YAP led to impaired T cell expansion compared with those receiving a control vector (Fig. 3 E), along with decreased IFN-γ and IL-2 production and CD44 expression (Fig. 3 F). Thus, expression of WT-YAP in YAP-deficient T cells rescues the WT phenotype.

Taken together, T cells ramp up expression of YAP after activation over 24 h (Fig. 1 D), and in LCMV infection, the LN microenvironment is soft during this period (Fig. 1 A). Thus, whether priming in vitro or in the infection model, the presence of YAP in T cells being activated in a mechanically soft environment checks immune responses.

YAP inhibits metabolic reprogramming of activated T cells

In other cell types, YAP plays a role downstream of metabolic sensors to allow proliferation only when there are ample metabolic resources (Koo and Guan, 2018). YAP activity can also regulate the metabolic state of a cell to support a proliferative program (Cox et al., 2016; Bertero et al., 2016). The metabolic state of T cells is tightly regulated and central to their responses. We observed an increase in glycolytic capacity in activated YAPcKO T cells compared with littermate controls (Fig. 4 A). However, there were no differences in basal glucose uptake or

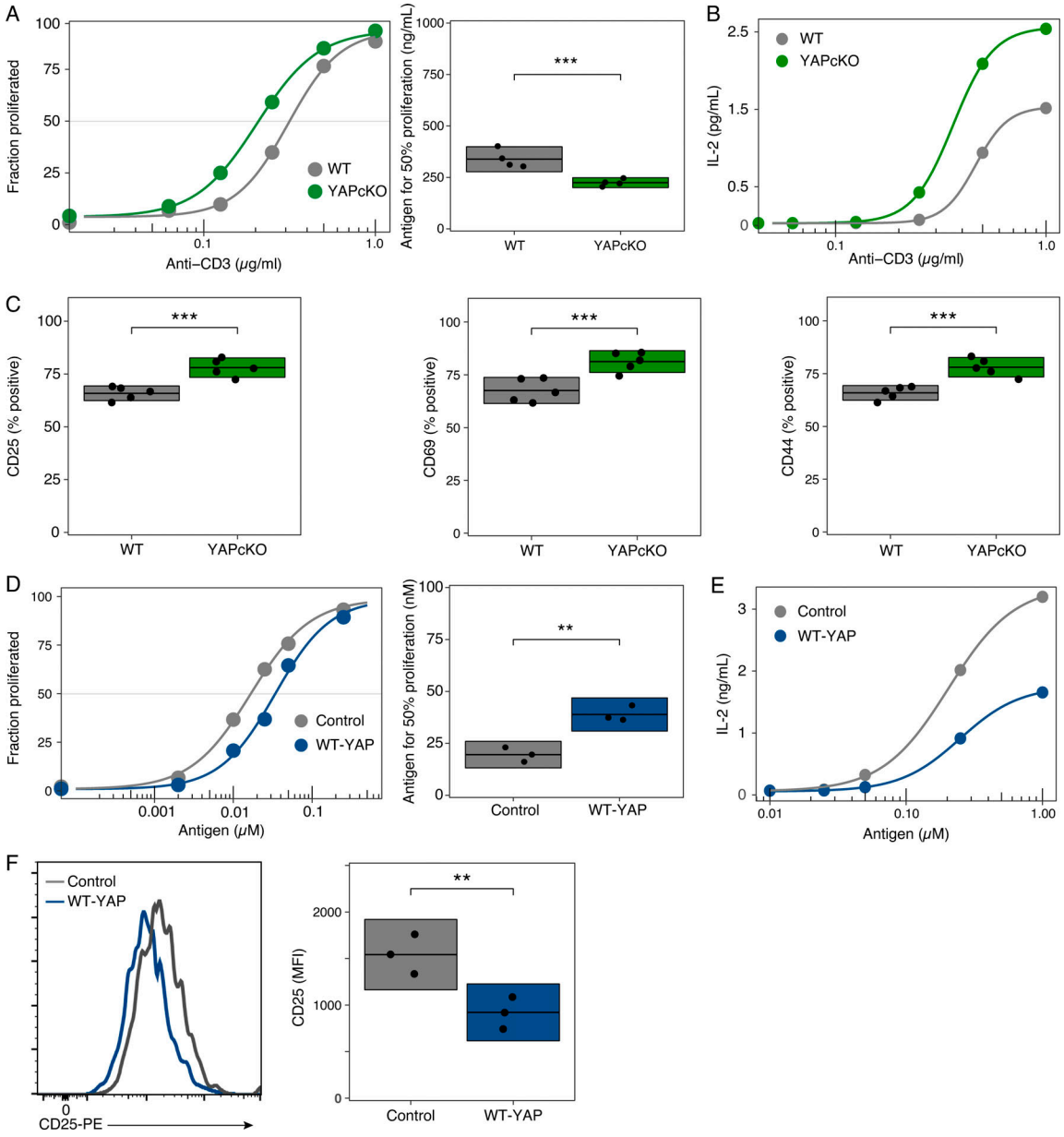

Figure 2. **YAP restrains T cell proliferation and effector function. (A)** Proliferation (left) of CFSE-labeled WT (gray) or YAPcKO (green) T cells after anti-CD3 and anti-CD28 stimulation. ED_{50} calculated from four independent dose–response experiments shown (right). Box shows mean and 95% CI. **(B)** IL-2-secretion of WT or YAPcKO T cells at 72 h after activation with anti-CD3 and anti-CD28 stimulation. Data representative of three independent experiments. **(C)** Activation markers of WT or YAPcKO T cells stimulated with 1 µg/ml anti-CD3 for 24 h. Data from five independent experiments are shown. Box shows mean and 95% CI. **(D)** Proliferation of CellTrace Violet–labeled OT-II YAPcKO T cells transduced with control vector (gray) or WT-YAP (blue) after restimulation with WT splenocytes and OVA peptide 323–339. ED_{50} calculated from three independent dose–response experiments shown (right). Box shows mean and 95% CI. **(E)** IL-2 secretion of OT-II YAPcKO T cells transduced with control vector (gray) or WT-YAP (blue) at 48 h after restimulation with OVA peptide. Data representative of two independent experiments. **(F)** CD25 expression of restimulated T cells from experiment in E. Data from three independent experiments are shown. Box shows mean and 95% CI. Permutation P values: **, P < 0.01; ***, P < 0.001.

basal glycolysis (Fig. S3, A and B). Further, YAPcKO T cells exhibited a greater level of mitochondrial respiratory capacity (Fig. 4 B). Absence of YAP also led to elevated basal level of oxygen consumption rate (OCR) and spare respiratory capacity, indicators of the mitochondrial ability to respond to stress (van der Windt et al., 2013; Fig. S3 C). Effector WT and YAPcKO T cells were notably different in regard to basal extracellular acidification rate (ECAR)/OCR ratio and in their maximal glycolytic and respiratory capacity (Fig. S3 E). On the other hand, we saw the basal ECAR and OCR of naive cells were nearly identical, consistent with the lack of YAP expression in naive T cells (Fig. S3, D and E). There was more mitochondrial staining in YAPcKO effector T cells compared with WT T cells (Fig. 4 C), which explained the increased respiratory capacity. We also found a higher mitochondrial membrane potential in YAPcKO effector T cells compared with that of WT T cells (Fig. 4 D),

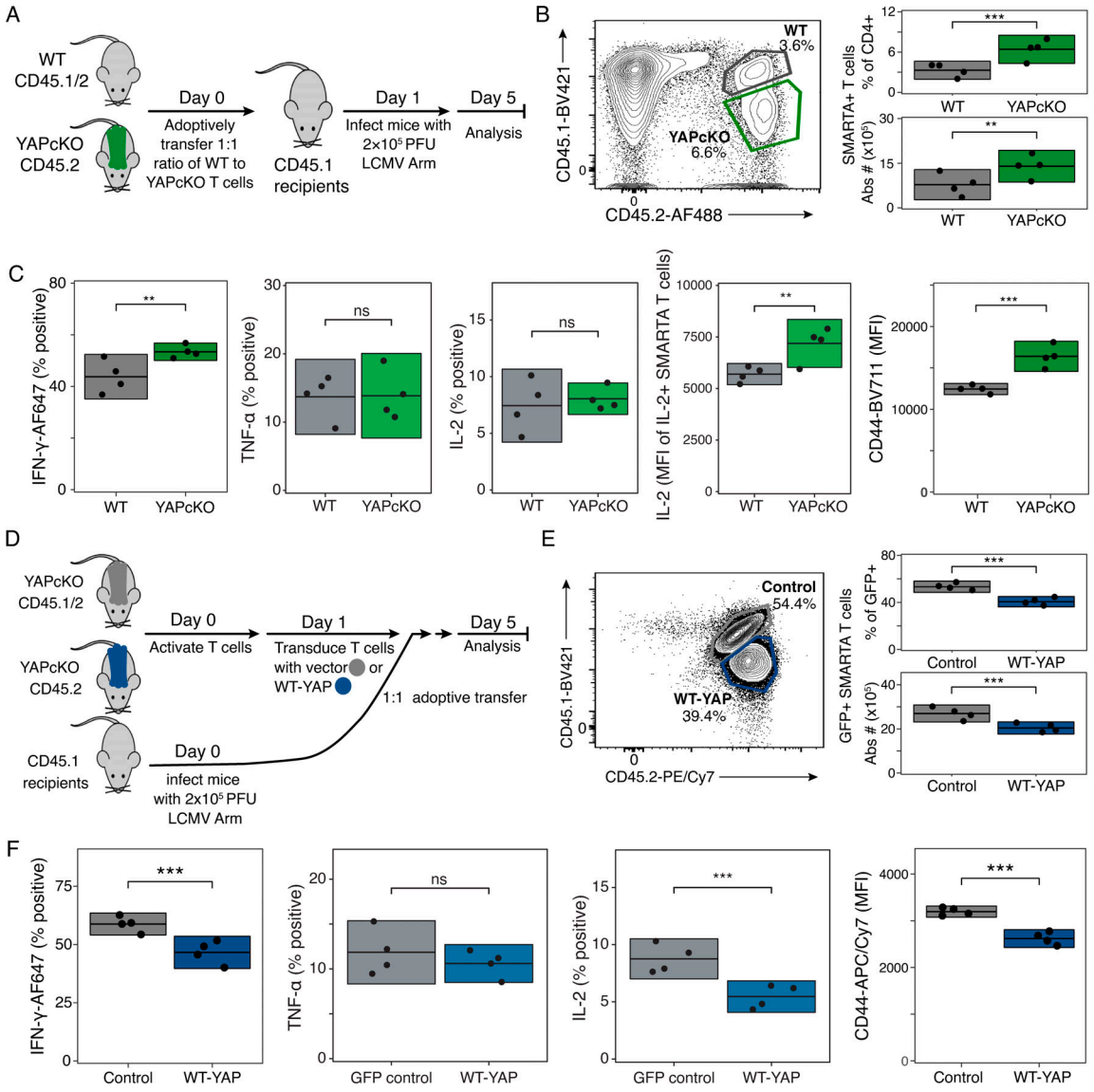

Figure 3. **YAP suppresses the T cell antiviral response. (A)** Schematic of LCMV adoptive transfer model. **(B)** The frequency of adoptively transferred SMARTA WT (gray) and YAPcKO T cells (green) in mice on day 5 after infection with LCMV. Data are representative of four independent experiments (n = 4 in each group in each experiment). Box shows mean and 95% CI. **(C)** Quantification of intracellular cytokine expression (% positive of SMARTA T cells), CD44 mean fluorescence intensity (MFI), and IL-2 MFI of adoptively transferred YAPcKO SMARTA T cells from experiment in A. Each dot represents an independent experiment. Boxplot shows mean and 95% CI. **(D)** Schematic of LCMV adoptive transfer model with retroviral transduction. **(E)** The frequency of adoptively transferred SMARTA YAPcKO T cells transduced with control vector (gray) or WT-YAP (blue). Data are representative of three independent experiments (n = 4 in each group in each experiment). Box shows mean and 95% CI. **(F)** Quantification of intracellular cytokine expression (% positive of GFP⁺ T cells) and CD44 MFI in YAP shRNA T cells from experiment in D. Abs, antibodies; ns, not significant. Permutation P values: **, P < 0.01; ***, P < 0.001.

which has been linked to increased ATP production and T cell effector function (Sukumar et al., 2016). Thus, YAP plays a role upstream of the metabolic program of effector T cells.

Metabolomics experiments demonstrated large differences between polar metabolite levels in WT and YAPcKO effector T cells (Fig. 4 E). Differential metabolites in the first principal component included the ADP/ATP and AMP/ATP ratios, amino acids, citric acid cycle intermediates, and nucleotides (Fig. S3 G). We also observed significant differences in the end-products of metabolic activity, including elevated intracellular lactate and ATP (Fig. S3 F). The citric acid (TCA) cycle fuels oxidative phosphorylation, and so we examined TCA cycle intermediates and found a substantial increase in YAPcKO T cells as compared with controls (Fig. 4 F). To determine if YAPcKO effector T cells had more TCA cycle intermediates because of an increased rate of cycling, we used metabolic tracing. After incubating effector T cells with ^{13}C-glucose or ^{13}C-glutamine, we did not detect a significant difference in the isotopomeric labeling of citrate for ^{13}C-glucose–treated or ^{13}C-glutamine–treated samples, indicating that YAPcKO T cells had similar rates of TCA cycling to WT T cells (Fig. S3 H). Indeed, the fractional contribution of ^{13}C-labeled glucose to isotopologues of TCA metabolites was mostly similar between WT and YAPcKO T cells (Fig. S3 I). These labeling results suggest that the higher levels of TCA metabolites

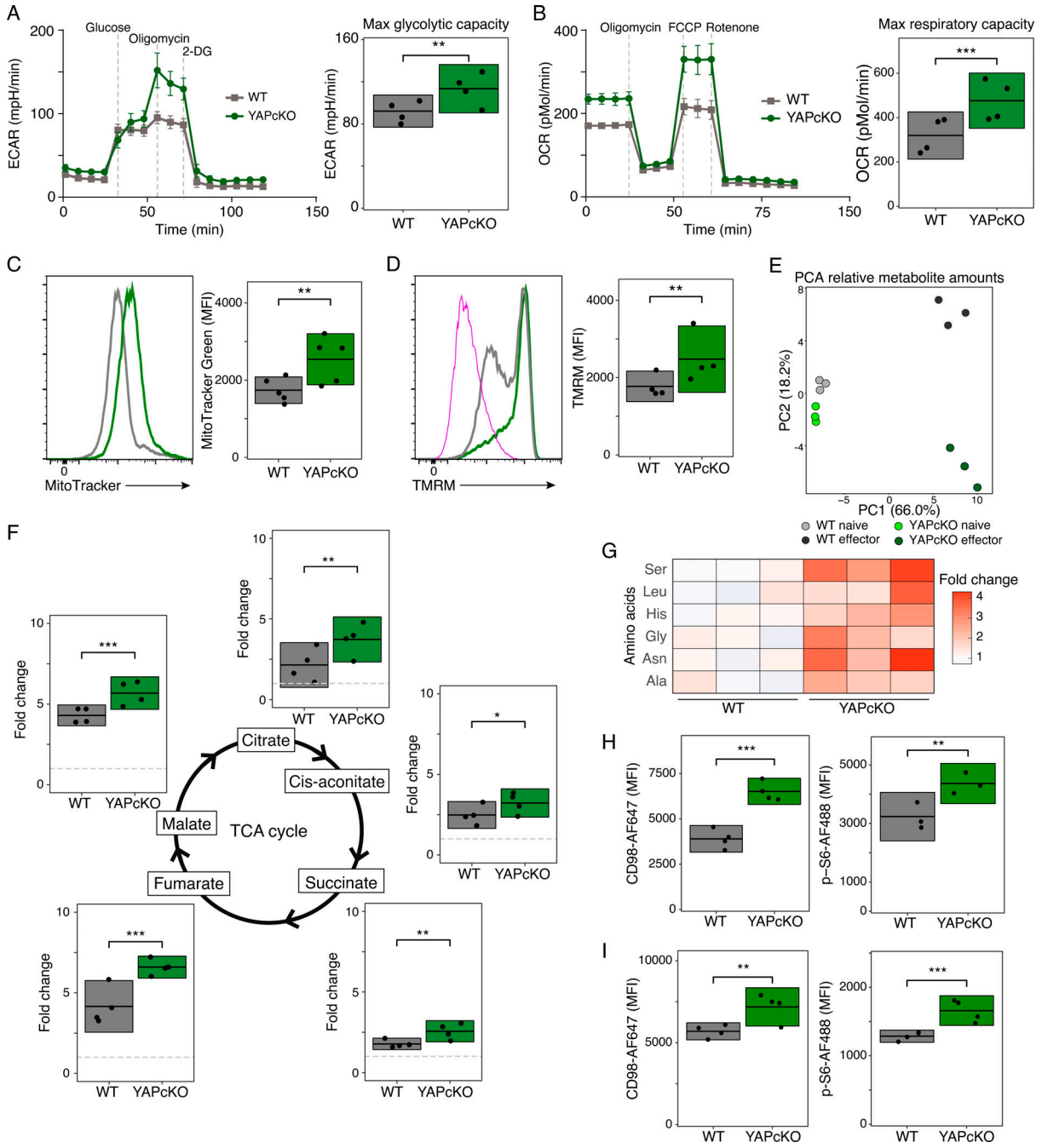

Figure 4. **YAP inhibits metabolic reprogramming and amino acid metabolism. (A)** ECAR of WT (gray) and YAPcKO (green) effector T cells on day 3 after activation under basal conditions and in response to glucose, oligomycin, and 2-DG. Four such independent experiments are shown. Box shows mean and 95% CI (right) of MGC. **(B)** OCR of WT (gray) and YAPcKO (green) effector T cells on day 3 after activation under basal conditions and in response to oligomycin, FCCP, and rotenone/antimycin A. Four such independent experiments are shown. Box shows mean and 95% CI (right) of maximal respiratory capacity. **(C)** WT or YAPcKO effector T cells were analyzed for mitochondria size with MitoTracker Green. Data from five independent experiments are shown. Box shows mean and 95% CI. **(D)** WT or YAPcKO effector T cells analyzed for mitochondria membrane potential measured using tetramethylrhodamine methyl ester perchlorate (TMRM). FCCP (magenta) was used as a control to ensure mitochondria were depolarized. Data from four independent experiments are shown. Box shows mean and 95% CI. **(E)** Metabolomics of naive and effector WT/YAPcKO T cells. Principal component analysis (PCA) shows relationships among WT and YAPcKO T cells. Data shown are from a collection of three independent experiments. **(F)** Fold change of intracellular TCA metabolites measured by mass spectrometry between effector WT and YAPcKO T cells normalized to naive WT or YAPcKO T cell levels (gray dotted line), respectively. Data from four independent experiments are shown. Box shows mean and 95% CI. **(G)** Heatmap of intracellular amino acid abundance. Intracellular amino acid abundance in WT or YAPcKO effector T cells was first normalized to their respective naive counterparts. Data are shown as fold change of intracellular amino acid abundance in WT or YAPcKO effector T cells normalized to the average abundance of each amino acid in WT T cells from three independent experiments. **(H)** CD98 and p-S6 expression in WT (gray) and YAPcKO (green) effector T cells activated in vitro, showing four independent experiments (three for p-S6). Box shows mean and 95% CI. **(I)** CD98 and p-S6 expression in adoptively transferred WT and YAPcKO SMARTA T cells in mice 5 d after infection with LCMV. WT (gray) and YAPcKO (green) effector T cells. Data are representative of three independent experiments (n = 4 in each group in each experiment). Each dot is one mouse within an experiment. Box shows mean and 95% CI. Permutation P values: *, P < 0.05; **, P < 0.01; ***, P < 0.001.

in YAPcKO T cells are due to increased mitochondrial biogenesis rather than enhanced mitochondrial function.

YAP coordinates amino acid metabolism and mammalian target of rapamycin (mTOR) activity

Our metabolomics data revealed that YAPcKO effector T cells had higher intracellular amounts of several amino acids, including alanine, serine, glycine, asparagine, and leucine, all of which have been implicated in T cell effector function and proliferation (Fig. 4 G and Fig. S3 J; Ma et al., 2017; Sinclair et al., 2013; Ron-Harel et al., 2019). In line with the intracellular data, the abundance of these amino acids in the media was markedly reduced in the supernatant of cultured YAPcKO T cells compared with controls (Fig. S3 K).

We asked if the elevated amino acids were imported directly or arose anabolically from imported glucose. CD98 (SLC3A2) forms a complex with LAT1 (SLC7A5) for the import of several amino acids, including leucine, and is a critical metabolic checkpoint for activated T cells (Sinclair et al., 2013). CD98 expression was higher in YAPcKO effector T cells than WT controls (Fig. 4 H). Thus, during T cell activation, YAPcKO T cells imported more amino acids from the extracellular environment. In examining mass isotopomer distributions of amino acids after ^{13}C-glucose labeling, we did not detect any significant differences, indicating that the elevation of intracellular amino acids in YAPcKO T cells was not due to glucose import (Fig. S3 L).

Amino acid import leads to critical mTOR signaling in activated T cells (Sinclair et al., 2013). To test the involvement of mTOR in the YAP-mediated effects on T cell metabolism, we examined downstream targets of mTOR in effector T cells. Indeed, phosphorylation of S6 was greater in YAPcKO effector T cells (Fig. 4 H). To determine whether elevated amino acid transport and mTOR activity also held true in an in vivo setting, we measured the expression of CD98 and p-S6 in adoptively cotransferred SMARTA T cells (WT and YAPcKO) after 5 d of infection with LCMV. YAPcKO SMARTA effector T cells had more CD98 and p-S6 than controls (Fig. 4 I). These data show that one way YAP dampens the T cell response is by downregulating amino acid transport and mTOR activation.

YAP regulates the interaction of IQGAP1 and NFAT1

Regulation of many metabolic changes in effector T cells have been attributed to transcription driven by NFAT (Klein-Hessling et al., 2017; Vaeth et al., 2017). Furthermore, store-operated calcium entry and calcineurin regulate mitochondrial activity in an NFAT-dependent manner (Vaeth et al., 2017). Upon triggering of the T cell receptor, NFAT1 and NFAT2 travel into the nucleus and drive transcription of targets such as IL-2. Given the metabolic changes and the increased IL-2 expression of YAPcKO T cells, we studied the activation of NFAT1 and NFAT2. YAP-deficient effector T cells exhibited greater NFAT1, but not NFAT2, nuclear localization compared with controls (Fig. 5 A).

The NFAT-scaffolding protein IQGAP1 was recently shown to interact with YAP (Sayedyahossein et al., 2016). We hypothesized that in T cells, YAP could interact with IQGAP1 and thus regulate IQGAP1's interactions with NFAT1. We first sought to determine if YAP directly interacted with IQGAP1. We transduced FLAG-tagged YAP into YAPcKO T cells and demonstrated a specific YAP-IQGAP interaction (Fig. 5 B). NFAT1 was not clearly coimmunoprecipitated in this complex.

We hypothesized that in T cells, YAP could regulate the ability of IQGAP1 to bind to phosphorylated NFAT1, and thus regulate NFAT1 nuclear translocation. We made mutants of YAP (Fig. 5 C) and tested their interactions with IQGAP1 and their effects on NFAT1 translocation. Significantly more NFAT1 immunoprecipitated with IQGAP1 in YAPcKO T cells transduced with WT-YAP compared with control, showing that YAP augments the interaction between IQGAP1 and NFAT1 (Fig. 5 D).

In the canonical Hippo pathway that regulates YAP, the LATS1/2 kinases respond to biomechanical inputs and phosphorylate YAP, sequestering it in the cytoplasm (Misra and Irvine, 2018). On the other hand, unphosphorylated YAP is capable of nuclear localization under mechanical force (Elosegui-Artola et al., 2016, 2017). To test whether Hippo activity is important for YAP function in T cells, we mutated four of the five LATS1/2-targeted serine sites to alanine (human sequence numbers S61A, S109A, S127A, and S164A, called YAP-4SA). Another post-translational modification that controls YAP trafficking is O-linked glycosylation of Ser109, mutated to Ala in our 4SA construct, which is required for nuclear transport in some cells (Peng et al., 2017). YAPcKO T cells expressing YAP-4SA had significantly more NFAT1 associated with IQGAP1 compared with empty vector, and similar levels of bound NFAT1 as T cells expressing WT-YAP (Fig. 5 D). This result shows that YAP influences the interaction of IQGAP1 and NFAT1, and that this interaction is not regulated by O-linked glycosylation or by most of the LATS1/2 phosphorylation sites in T cells.

Ser397 of YAP mechanoregulates interaction with IQGAP1 and NFAT1

We further mutated Ser397 into alanine in addition to the mutations in YAP-4SA and termed this mutant YAP-5SA. This serine is phosphorylated by the Hippo pathway kinases LATS1/2 in response to biomechanical cues (Mo, 2017; Misra and Irvine, 2018). In contrast to YAP-4SA, YAPcKO T cells expressing YAP-5SA failed to keep NFAT1 coupled to IQGAP1 (Fig. 5 D). To further refine whether this serine plays a role in the interaction of YAP and IQGAP1, we looked for an association between FLAG-tagged YAP-4SA or YAP-5SA and IQGAP1 (Fig. 5 B). There was a twofold higher association between IQGAP1 and YAP-4SA than YAP-5SA. Thus, Ser397 promotes binding of both YAP and NFAT1 with IQGAP1.

To clarify the role of Ser397 in regulating the interaction of IQGAP1 and NFAT1 and add a mechanistic understanding of how stiff and soft microenvironments influence YAP activity, we studied Ser397 in stiff and soft environments. We activated YAPcKO T cells and virally transduced with FLAG-tagged WT-YAP. Then we placed T cells upon stiff or soft matrices as before with antigen-pulsed splenocytes. In mechanically soft environments, Ser397 is twice as phosphorylated as in stiff environments (Fig. 5 E). Thus, YAP Ser397 is post-translationally modified by phosphorylation in soft environments.

The YAP transcriptional enhanced associate domain (TEAD)–binding domain (TBD) plays a critical role in the

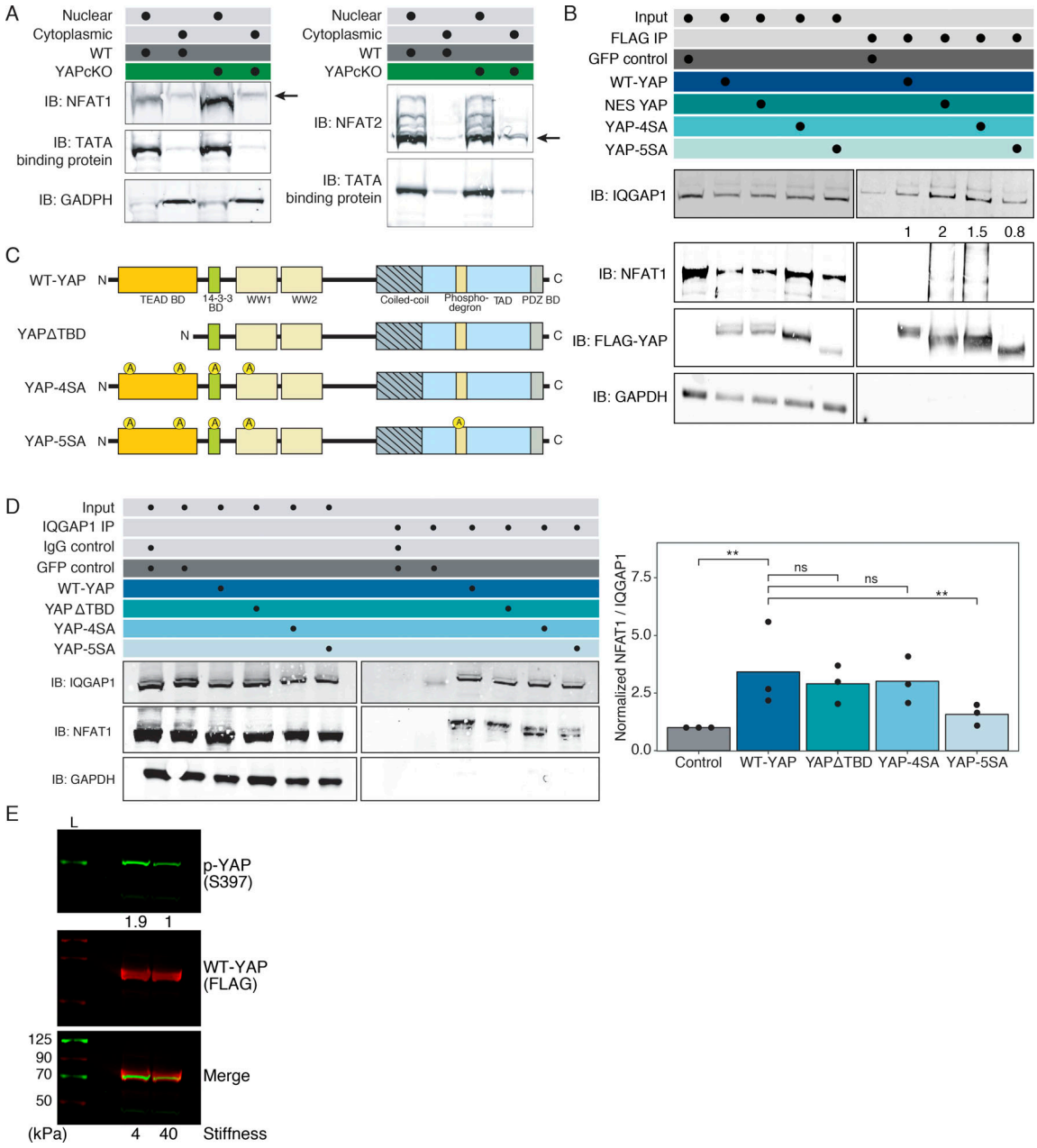

Figure 5. **YAP regulates the interaction of IQGAP1 and NFAT1. (A)** Immunoblot analysis for NFAT1 and NFAT2 in nuclear (N) and cytoplasmic (C) fractions of effector WT (gray) and YAPcKO (green) T cells. Cytoplasmic GAPDH and nuclear TATA-binding protein served as loading and fractional controls. Data are representative of three independent experiments (for NFAT1). **(B)** Co-immunoprecipitation analysis of proteins with anti-FLAG in YAPcKO T cells transduced with FLAG-tagged human WT-YAP, NES YAP, YAP-4SA, YAP-5SA, or GFP control. Immunoblotted proteins include IQGAP1, NFAT1, FLAG, and GAPDH. IQGAP1 pulled down was quantified by first normalizing to IQGAP expressed in the whole-cell lysate and then to FLAG-YAP pulled down. Data representative of two independent experiments. **(C)** Schematic representation depicting the domain architecture and YAP mutants used in the study. **(D)** Co-immunoprecipitation analysis of proteins with anti-IQGAP1 in YAPcKO T cells transduced with WT-YAP, YAPΔTBD, YAP-5SA, YAP-4SA, or GFP control. Immunoblotted proteins included IQGAP1, NFAT1, and GAPDH. Data representative of three independent experiments (dots at right). Quantification of NFAT1 pulled down was normalized to the ratio of NFAT1 to IQGAP1 pulled down in the control. **(E)** Western blot of Ser397 phosphorylation in SMARTA YAPcKO T cells transduced with FLAG-tagged WT-YAP and restimulated on stiff or soft scaffolds with WT splenocytes plus 30 nM SMARTA peptide. Relative phosphorylation of Ser397 shown, normalized to total YAP (FLAG) and stiff condition. L, molecular weight (MW) ladder. Data representative of two independent experiments. IB, immunoblot. Permutation P values: **, $P < 0.01$; ns, not significant.

transcriptional regulation enacted by YAP in other systems, but the TBD is not necessarily required for all YAP-associated biology (Wang et al., 2017). To explore whether the TBD was required for IQGAP1 regulation of NFAT1, we expressed YAPΔTBD in YAPcKO T cells. There was a similar amount of NFAT1 associated with IQGAP1 compared with T cells transduced with WT-YAP or YAP-4SA (Fig. 5 D). Thus, the YAP TBD does not regulate IQGAP1–NFAT1 interactions.

Taken together, these results show that Ser397 of YAP is phosphorylated in the soft microenvironment, and promotes the association of NFAT1 with its scaffold IQGAP1.

Mechanics, YAP, and IQGAP1 interactions regulate the nuclear localization of NFAT1

To assess the relevance of this newly revealed influence of YAP on the association of IQGAP1 and NFAT1, we sought next to study the regulation of the nuclear localization of NFAT1, especially in context of the mechanical microenvironment. To correlate the subcellular/nuclear localization, mechanics, and the kinetics of expression of YAP, IQGAP1, and NFAT1, we activated WT T cells on stiff and soft substrates. Maximum YAP expression occurred on day 3, and was diminished by day 6. (Fig. S4 A). YAP localization was decidedly more nuclear in the stiff microenvironment, regardless of the day (Fig. S4 B). NFAT1 expression also peaked on day 3 after activation, and its expression was slightly enhanced in the stiff conditions (Fig. S4 C). NFAT1 exhibited greater nuclear localization in the stiff environment versus the soft environment (Fig. S4 D), with the largest difference on day 3. Expression of IQGAP1 was consistent over the course of the experiment (Fig. S4 E), and IQGAP1 had almost no presence in the nucleus (Fig. S4 F), consistent with previous work showing that IQGAP1 is cytoplasmic (Sharma et al., 2011). These results show the kinetics of expression and localization of YAP, NFAT1, and IQGAP1. The findings reveal the correlation that when YAP expression is highest, on day 3, NFAT1 was most suppressed from nuclear localization in the soft versus stiff microenvironment. Thus, YAP activity and the effects on NFAT1 were influenced by the mechanical environment.

To assess the mechanism by which the interaction of YAP and IQGAP1 could functionally alter the nuclear localization of NFAT1, we transduced the YAP constructs into YAPcKO T cells and stained for NFAT1 and YAP. In YAPcKO cells expressing WT-YAP, YAP-4SA, or YAPΔTBD, NFAT1 was suppressed from nuclear localization to a similar degree (Fig. 6, A and B). In contrast, we saw normal NFAT1 nuclear localization with the YAP-5SA construct, similar to cells transduced with the control vector. Thus, YAP regulates the localization of NFAT1 into the nucleus, and the TBD of YAP does not play a role in this regulation. However, when YAP Ser397 is mutated, YAP was unable to keep NFAT1 from the nucleus.

We sought to better understand the subcellular location where YAP influences IQGAP1. In other cells, YAP drives biological responses in the nucleus. However, in T cells, YAP-mediated suppression of NFAT1 nuclear localization was preferentially associated with cytoplasmic, not nuclear, localization (Fig. S4 B). To further probe the necessity of YAP to be localized in the cytoplasm, we prepared constructs with FLAG-YAP tagged with a nuclear exclusion sequence (NES) or nuclear localization sequence (NLS). We validated through confocal microscopy that NES-YAP was largely excluded from the nucleus and NLS-YAP was enriched in the nucleus compared with WT YAP (Fig. 6 C). We examined if forcing the localization of YAP to the cytoplasm could influence its interaction with IQGAP1. We looked at coimmunoprecipitation of FLAG-NES-YAP with IQGAP1 and found that there was twice as much association for NES-YAP than WT YAP (Fig. 5 B). We manipulated the cytoplasmic localization of YAP to examine the effect on NFAT1 localization. YAPcKO T cells transduced with NES-YAP have less nuclear NFAT1 than control transduced T cells, while YAPcKO cells transduced with NLS-YAP have more nuclear NFAT1 than control transduced T cells (Fig. 6 D). Thus, YAP acts in the cytoplasm to control the subcellular localization of NFAT1.

We assessed the immunological impact of these YAP constructs and their regulation of NFAT1 by examining the proliferation of $CD4^+$ T cells. YAPcKO T cells transduced with WT-YAP or YAPΔTBD (i.e., those with intact Ser397) proliferated less after restimulation than those transduced with control vector or YAP-5SA (lacking Ser397; Fig. 6, E and F). These results offer biological demonstration that regulation of NFAT1 by YAP (and its Ser397) in T cells regulate effector responses.

Taken together, these results show that YAP interacts directly with IQGAP1 in the cytoplasm and subsequently regulates the IQGAP1–NFAT1 interaction. Ser397 of YAP plays a central role for these interactions. In mechanically soft environments, Ser397 is phosphorylated, which promotes its interaction with IQGAP1. In mechanically stiff environments, Ser397 is less phosphorylated, facilitating nuclear transport (Elosegui-Artola et al., 2017).

We questioned whether the role YAP played in suppressing T cell responses was primarily mediated through NFAT. YAP has many potential partners and in other systems regulates transcription through interaction with TEADs factors in the nucleus. In T cells, however, YAP-mediated suppression of responses was associated with cytoplasmic, not nuclear, localization. Furthermore, deletion of the TBD of YAP did not affect interaction with IQGAP1, translocation of NFAT1 to the nucleus, translocation of YAP to the nucleus, or proliferative responses of T cells. To identify any potential non-NFAT1 influence on YAP, we employed a strategy to modestly suppress NFAT1 while comparing activation of T cells from WT and YAPcKO mice. If YAP played an inhibitory role aside from on NFAT1, we would expect to see WT T cells inhibited beyond YAPcKO T cells at all levels of NFAT1 suppression. We stimulated T cells using a modest antigen dose to allow for suppression, co-cultured with calcineurin inhibitor cyclosporine-A (CsA). In the absence of CsA, YAPcKO T cells showed greater activation than WT controls. At low doses of CsA (10–25 nM), while activation was mostly still intact, YAPcKO T cells showed a diminishment of CD25 and CD98 expression to match the levels of WT effector T cells (Fig. 6, G and H). Above this dose, we observed that WT and YAPcKO T cells showed a lockstep decrease in effector responses, down to complete suppression of activation at high CsA. Any YAP-dependent, NFAT1-independent suppression of T cell activation should not allow this effect. Thus, these data indicate that YAP suppresses T cell effector responses through an NFAT-dependent mechanism.

Mechanoregulation of NFAT1 requires YAP

These data led us to hypothesize that the mechanical microenvironment controlled NFAT1 activity in T cells through YAP, and specifically through Ser397 in YAP. We first compared NFAT1 nuclear/cytoplasmic expression in WT SMARTA T cells activated by peptide-loaded APCs on soft and stiff scaffolds. We found significantly increased nuclear NFAT1 in T cells activated on the stiff microenvironment as compared with soft, suggesting

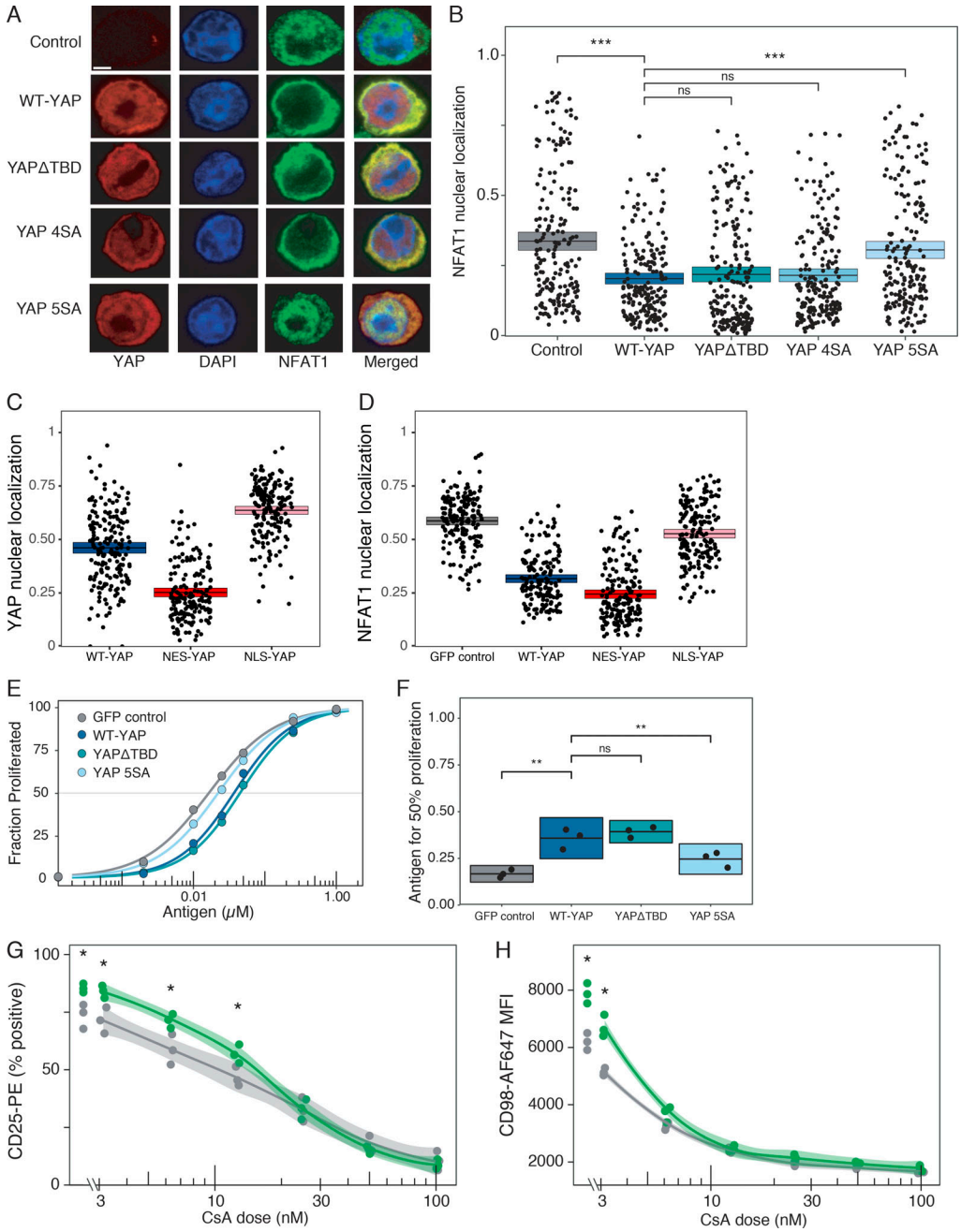

Figure 6. **YAP regulates the nuclear localization of NFAT1. (A and B)** YAPcKO T cells were transduced with human WT-YAP, YAPΔTBD, YAP-5SA, YAP-4SA, or GFP control, sorted for GFP-positive cells, and then stained for immunofluorescence. Representative images show NFAT1 localization for each condition. Scale bar, 2 µm. **(B)** Quantification of NFAT1 nuclear localization. Each data point represents a single cell, n > 200 per condition. Data representative of three independent experiments. Box shows mean and 95% CI. **(C and D)** YAPcKO T cells were transduced with human WT-YAP, NES YAP, NLS YAP, or GFP control, sorted for GFP-positive cells, then stained for immunofluorescence and assessed for colocalization of either YAP (C) or NFAT1 (D) with DAPI. Each point represents a single T cell. Data are representative of two experiments, n > 150 each condition. Each dot is a T cell. Box shows mean and 95% CI. **(E)** Dose response of CellTrace Violet–labeled OT-II YAPcKO T cells transduced with control vector, WT-YAP, YAP 5SA, or YAPΔTBD and restimulated with OVA peptide 323–339 to measure proliferation. Data shown are representative of three independent experiments, which are aggregated in F. **(F)** The amount of peptide required for 50% proliferation (ED_{50}) was calculated from each dose response curve. Each dot is an independent experiment. Box shows mean and 95% CI. **(G and H)** Flow-cytometric analysis of CD25 (G) or CD98 (H) expression in WT (gray) and YAPcKO (green) T cells treated with differential concentrations of CsA. Data from three independent experiments are shown. ns, not significant. Permutation P values: *, P < 0.05; **, P < 0.01; ***, P < 0.001.

that mechanical forces supervise NFAT1 activity (Fig. 7 A). Importantly, the effect of elastic modulus on NFAT1 localization was entirely abolished in YAPcKO T cells (Fig. 7 A). NFAT1 localization for YAPcKO T cells was in fact comparable to the WT stiff condition (Fig. 7 B). In addition, the amino acid transporter CD98, a known transcriptional target of NFAT (Klein-Hessling et al., 2017), was up-regulated in WT SMARTA T cells activated on stiff surfaces compared with that of soft surfaces (Fig. 7 C),

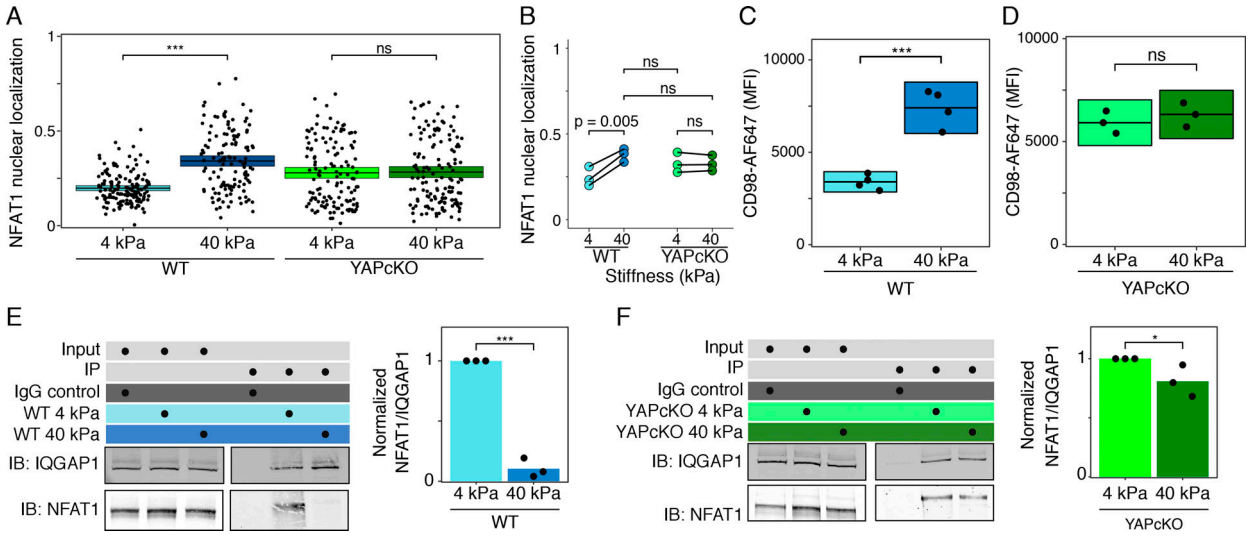

Figure 7. **YAP mechanoregulates NFAT1 activity. (A and B)** T cells from WT or YAPcKO SMARTA strains activated on soft (4 kPa) and stiff (40 kPa) alginate-RGD hydrogels were imaged for NFAT1 by microscopy. Each dot represents a single T cell, $n > 200$ per condition. Box shows mean and 95% CI. Data from three independent experiments shown (B). Each dot represents the bootstrap mean nuclear localization. **(C and D)** CD98 expression of (C) WT or (D) YAPcKO T cells activated on soft and stiff alginate-RGD matrices. Each dot shows one independent experiment. Box shows mean and 95% CI. **(E and F)** Co-immunoprecipitation analysis of IQGAP1 in (E) WT SMARTA T cells or (F) YAPcKO SMARTA T cells activated on soft and stiff substrates. Immunoblotted proteins included IQGAP1 and NFAT1. Data representative of three independent experiments (dots at right). Quantification of NFAT1 pulled down was normalized to IQGAP1 pulled down in each experiment and normalized to 4 kPa experiment. ns, not significant. Permutation P values: *, $P < 0.05$; **, $P < 0.01$; ***, $P < 0.001$.

whereas YAPcKO SMARTA T cells exhibited comparable expression of CD98 when activated on stiff versus soft microenvironments (Fig. 7 D). These results indicate that NFAT1 localization and activity are dependent on mechanics and YAP in T cells.

To test if substrate stiffness had a direct effect on the amount of YAP bound to IQGAP1 to control NFAT1 activity, we recovered T cells from soft and stiff scaffolds after activation and coimmunoprecipitated proteins complexed with IQGAP1. Much less NFAT1 was bound to IQGAP1 in T cells seeded on stiff scaffolds versus soft scaffolds (Fig. 7 E). In contrast, NFAT1 was found complexed with IQGAP1 to a similar degree in YAPcKO T cells regardless of scaffold stiffness (Fig. 7 F). Thus, the mechanical environment influences NFAT1 nuclear localization, activation markers, proliferation, and IQGAP1–NFAT1 interaction in a YAP-dependent manner.

To assess the global impact of YAP on NFAT1 regulation in the context of tissue mechanics, we identified NFAT-regulated genes (Martinez et al., 2015) in WT and YAPcKO T cells activated on soft or stiff surfaces. WT T cells demonstrated stiffness-dependent, differential regulation of many NFAT1-dependent genes, but YAPcKO T cells failed to show the same (Fig. 8 A). Many of the differentially expressed genes mapped to metabolic processes, ribosomal biogenesis pathways, and extracellular matrix–receptor interactions (Fig. 8 B). Altogether, our data indicate that YAP mechanoregulates NFAT1 and controls T cell activation in response to tissue mechanics.

Effector T cells leaving an activated LN may circulate into bystander LNs and tissues where autoantigens mimic a cognate stimulus. Molecular mimicry is indeed a major driver of autoimmunity that becomes primed during infections and arises clinically shortly thereafter (e.g., type 1 diabetes). Our model would suggest that the mechanical softness of bystander tissues should inhibit YAP-bearing effector T cells and suppress autoimmunity. To test this hypothesis, we assessed whether self-reactive YAP-deficient $CD4^+$ T cells could ignore the soft, inhibitory mechanical cues of unactivated LNs and tissues in vivo. We measured the ability of YAP to regulate type 1 diabetes in NOD.SCID mice, which lack functional T and B cells and thus have no pancreatic insulitis or lymphadenopathy. BDC2.5 T cells are diabetogenic when transferred into NOD.SCID mice, an outcome mediated by production of IFN-γ by activated T cells (You et al., 2003). We knocked down YAP in BDC2.5 T cells (Fig. 9 A) and transferred into NOD.SCID mice (Fig. 9 B). Mice receiving T cells depleted of YAP developed diabetes faster than with those receiving control T cells (Fig. 9 C). YAP-depleted BDC2.5 T cells developed into more IFN-γ^+ T cells on a per-cell basis than controls (Fig. 9 D), proliferated to a greater extent, and secreted more IL-2 (Fig. 9 E). These results show that tissue mechanics influence the effector phase of T cell responses. Specifically, the mechanically soft environment of the pancreatic islet attenuates T cell responses. These results indicate that sensing the mechanical microenvironment requires YAP to slow the progression of autoimmune disease.

Thus, in priming naive T cells during in vitro activation (Fig. 1) or in LCMV infection (Fig. 3), and in auto-reactive effector T cells in a model of autoimmune diabetes (Fig. 9), micromechanical softness sensed by the mechanosensor YAP attenuates T cell responses.

Discussion

Here, we identify a new physiological feedback mechanism whereby microenvironmental cues guide T cell effector

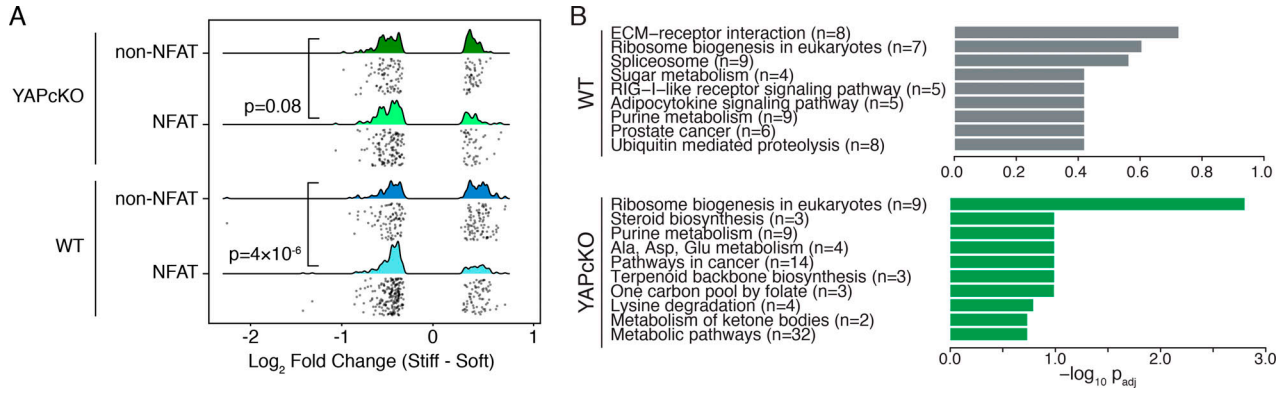

Figure 8. **YAP regulates NFAT-related genes and metabolic pathways. (A)** Differentially expressed genes from WT and YAPcKO T cells were mapped to NFAT1 and non-NFAT1 genes taken from a previous study (Martinez et al., 2015). Each dot represents a single gene. **(B)** Significantly enriched Kyoto Encyclopedia of Genes and Genomes pathways of differentially expressed genes in WT T cells experiencing soft versus stiff mechanical forces and in YAPcKO T cells experiencing soft versus stiff mechanical forces.

responses. These mechanical signals are separate from the mechanical forces exerted on the TCR, and thus T cells appear to be capable of independently sensing forces at both the molecular scale and tissue scale. The pathophysiological implication of these findings may extend from infections to autoimmunity to cancer, each of which shows considerable alterations in tissue mechanics. In this paper, we quantified the well-recognized changes in the mechanics of the LNs that occur during and after infections. Mechanical changes in LNs occur early due to migrating, activated dendritic cells that induce alterations in fibroblastic reticular cells (Acton et al., 2014; Astarita et al., 2015), and later from proliferation of lymphocytes within the encapsulated, confined environment. In a mechanically stiff microenvironment, YAP is preferentially localized in the nucleus, an effect mediated by regulation of nuclear pores (Elosegui-Artola et al., 2017). As activated T cells emigrate from the LN and the pathogen is cleared, the stiffness of LNs starts to fall. We describe a YAP-mediated pathway by which the mechanically soft microenvironment promotes quiescence: as YAP hampers NFAT1 nuclear transport and activity, it retards T cell activation and metabolic reprogramming (Fig. S5 A). Teleologically, we propose this mechanism may have evolved to tune down adaptive responses in post-infectious milieu and to reduce autoimmunity in bystander tissues.

This mechanism of YAP acting in the cytoplasm is distinct from other known roles of YAP, which promote transcription in the nucleus through TEADs (Totaro et al., 2018). In T cells, YAP is unlikely to play a similar role in the nucleus because we showed that deletion of the TBD does not affect its function (Fig. 5).

Thus, YAP controls the T cell's ability to recognize the rising and falling micromechanical environment, thereby modulating the metabolic state accordingly. The sensing of mechanics is not strictly dichotomous, and our studies suggest against the notion of an "optimal" stiffness but rather that the continuum of tissue rigidity offers a range of feedback to T cells. Whether in LN during priming or in peripheral tissues during effector phase, the T cell metabolic program is regulated by the mechanical environment. Our work thus identifies a new mechanical checkpoint by which the natural cycles of tissue mechanical changes directly fine-tune T cell activation and cellular bioenergetics.

Our work identified that YAP interacts with IQGAP1 in T cells, and leads to a state where interaction with NFAT1 is enhanced and thus nuclear transport of NFAT1 is diminished. IQGAP1 serves as a cytoplasmic scaffold for over 100 proteins and RNAs, and plays a central role in tethering three major functional components: kinases and phosphatases, proteasome components, and nucleocytoplasmic transporters. While we showed the interaction of YAP with IQGAP1 was direct, we speculate that their effect on regulating NFAT1 may be mediated through one or more of these associated proteins (Fig. S5 B). Indeed, knockdown of many of the components associated with IQGAP1 reduce NFAT1 association with IQGAP1 and increase NFAT1 activity in the nucleus; overexpression does the opposite (Willingham et al., 2005; Sharma et al., 2011). By using alanine mutants of the serines targeted by the LATS1/2 kinases, our studies support a mechanistic model that the micromechanical effects mediated by YAP require Ser397, a known target of the LATS1/2 kinases (Zhao et al., 2010) in response to mechanical cues (Mo, 2017; Fig. S5 B). Modulation of the LATS kinases themselves by extracellular matrix stiffness, cell–cell contact, cell stretch, shear forces, and other biomechanical cues has been well established (Misra and Irvine, 2018). In this work, we leveraged the discovery that the metabolic program of activated effector T cells is driven substantially by NFAT (Vaeth et al., 2017). Metabolic reprogramming in effector T cells of mTORC1, glycolysis, amino acid metabolism, and mitochondrial metabolism are all driven by NFAT. In our hands, YAP deficiency led to an increase in nuclear NFAT1 localization, transcriptional regulation of NFAT1-dependent genes, and metabolic changes that reflected increased NFAT1 activity. NFAT1 activity was reduced after overexpression of YAP and dissected further through the YAP mutants that alter interactions with IQGAP1. Thus, the suppression of the metabolic state by YAP in T cells is explained by decreased NFAT1 activity. NFAT–IQGAP interactions were promoted when YAP was present and in soft microenvironments, but regardless of mechanics, T cells bearing

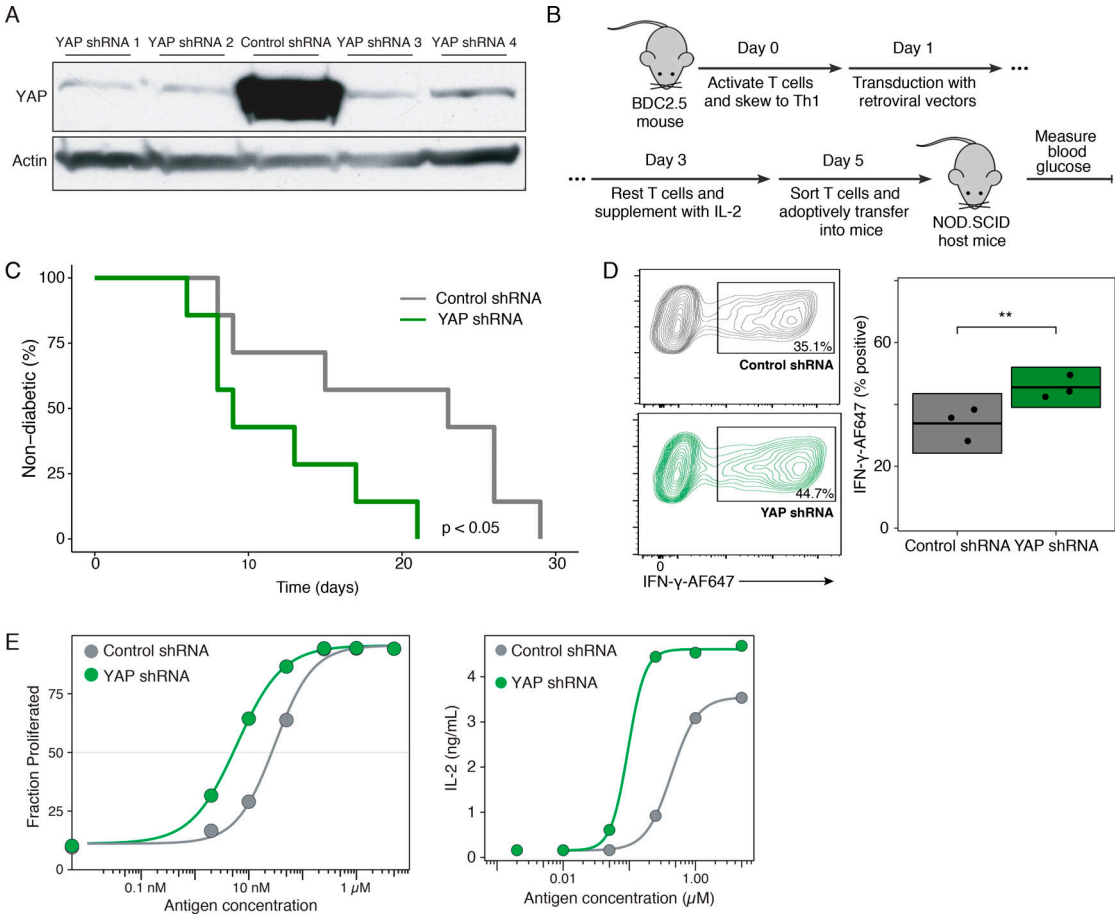

Figure 9. **YAP regulates autoimmunity. (A)** Immunoblot for YAP in T cells transduced with a control shRNA or one of four YAP different shRNAs. Data representative of two independent experiments. **(B)** Schematic of BDC2.5 type I diabetes adoptive transfer model. **(C)** Survival curve of NOD.SCID mice receiving T cells expressing either control or YAP shRNA (n = 7 mice per group). Representative of three independent diabetes experiments. **(D)** Percentage of restimulated BDC2.5 T cells producing IFN-γ after knockdown with control shRNA (gray) or YAP shRNA (green) in vitro. Data from three independent experiments are shown (right). Box shows mean and 95% CI. **(E)** Proliferation and IL-2 secretion of restimulated BDC2.5 T cells expressing YAP shRNA or control shRNA. Data representative of three independent experiments. Permutation P values: *, P < 0.05; **, P < 0.01; ***, P < 0.001.

YAP were hypoactive and hypometabolic compared with knockout T cells. Thus, we cannot strictly assess the relative contributions of YAP acting on mechanical cues versus playing a role in nonmechanically mediated suppression of effector functions when interpreting the in vivo responses seen in LCMV and T1D.

In other cell types, YAP collects critical regulatory cues to identify environments bearing favorable metabolic substrates and mechanics. We show that YAP also plays a role in the highly motile cells of the immune system, providing an accelerator or brake on T cell responses as they encounter infected and autoimmune tissue microenvironments. The results presented here demonstrate an orchestrated, molecular pathway allowing mechanical stiffness to modulate T cell metabolism. Our findings also newly reveal that the adaptive immune response is fine-tuned in accordance with physiological and pathophysiological changes in tissue mechanics.

Materials and methods

Mice

YAP flox ($YAP^{fl/fl}$) mice were kindly provided by F. Camargo (Boston Children's Hospital, Boston, MA). To generate cKO mice, $YAP^{fl/fl}$ mice were crossed to CD4-cre mice, resulting in mice lacking YAP in T cells (YAPcKO). YAPcKO mice were then crossed to TCR transgenic mice OT-II or SMARTA (kindly shared by S. Crotty; La Jolla Institute, La Jolla, CA). The OT-II TCR transgene recognizes the OVA peptide 323–339 (AnaSpec, AS-27024), while the SMARTA TCR transgene recognizes the mouse LCMV GP 61–80 peptide (AnaSpec, AS-64851). C57BL/6J (000664); B6.SJL 002014); CD4-cre (022071); OT-II (004194); BDC2.5 NOD (004460); and NOD.SCID (001303) mice were purchased from Jackson. Experiments were performed using mice between 6 and 10 wk of age. All mice were maintained in specific pathogen–free facilities and used according to protocols approved by the Stanford Administrative Panel on Laboratory Animal Care or the University of California, Los Angeles (UCLA) Animal Research Committee.

T cell isolation, activation, and proliferation

$CD4^+$ T cells were purified from murine spleen and LNs by EasySep immunomagnetic negative selection (StemCell Technologies, 19852). Unless otherwise specified, T cells were stimulated with 8 µg/ml plate-bound anti-CD3ε (clone 145-2C11 Bio X

Cell, BE0001-1) in media supplemented with 2 µg/ml anti-CD28 (clone 37.51 Bio X Cell, BE0015-1). For proliferation, T cells were incubated with 5 µM CellTrace CFSE (Thermo Fisher Scientific, C34554) or 5 µM CellTrace Violet (Thermo Fisher Scientific, C34517) in PBS + 0.1% BSA for 13 min at 37°C. T cells were then washed thrice with T cell media before (re)stimulation.

Retroviral transduction

T cells were transduced with retroviral vectors 24 h after activation. After 72 h, T cells moved to new plates lacking anti-CD3ε supplemented with 100 U/ml IL-2 (PeproTech, 200-02) and 5 ng/ml rmIL-7 (PeproTech, 200-07). After resting them for 48–72 h, the effector T cells were used for in vitro experiments or sorted by flow cytometry and used for adoptive transfer experiments.

YAP cDNA was kindly provided by J. Sage (Stanford University, Stanford, CA) and were cloned into murine stem cell virus (MSCV) retroviral vectors. Platinum E cells (Cell Biolabs, RV-102) were transfected with MSCV vectors containing WT YAP, YAPΔTBD, YAP 4SA, or YAP 5SA with T2A GFP. These vectors also contain the nonsignaling extracellular domain of human CD25 under control of the phosphoglycerate kinase 1 promoter. MSCV vectors containing only hCD25 and T2A-GFP were used as controls. 1 d after transfection, the medium was removed from the Platinum E cells and replaced with T cell medium. 2 d after transfection, viral supernatants were removed and concentrated ∼10-fold with Amicon Ultra-15 (EMD Millipore, UFC910024). Concentrated supernatants were added directly to wells containing T cell plus 8 µg/ml polybrene (Sigma-Aldrich, TR-1003-G) and spinfected at 800 *g* for 90 min at 37°C. Supernatants were removed, and T cell medium containing 100 U/ml IL-2 was added back to the wells.

For YAP knockdown experiments, Platinum E cells were transfected with an MSCV-based LTRmiR30-Puro-IRES-GFP–based vector (LMP; Open Biosystems). This retroviral vector had puromycin resistance removed but expressed GFP as a marker, and a miR-30-based shRNA hairpin targeting the following sequence in the 3′ untranslated region of YAP: 5′-AGTGAAGCT TCAGATGTA-3′. T cells were spinfected as above, except viral supernatants were not concentrated. As a control, the $CD4^+$ T cells were transduced with vectors containing an shRNA targeting CD8, as described (Chen et al., 2014). GFP^+ cells were flow-sorted, and knockdown of YAP was confirmed by Western blot.

Flow cytometry and reagents

For surface staining of cells, cells were blocked with anti-mouse CD16/32 TruStain fcX (BioLegend, 101320) for 5 min on ice before staining with surface antibodies at a 1:100 dilution. The following BioLegend antibodies were used for surface staining: CD4 (clones RM4-5 and GK1.5, 100532 and 100425); CD8 (clone 53–6.7, 100724); B220 (clone RA3-6B2, 103244); CD45.1 (clone A20, 110732, 110715); CD45.2 (clone 104, 109830, 109818, 109816); TCR Vα2 (clone B20.1, 127812), CD69 (clone H1.2F3, 104520, 104508); CD25 (clone PC61, 102017, 102007, 102020); CD44 (clone IM7, 103039, 103057, 103028); CD62L (clone MEL-14, 104418, 104435); CD98 (clone 4F2, 128207, 128210); and human CD25 (clone BC96, 302630, 302616). For intracellular cytokine staining, cells were fixed with cold 4% paraformaldehyde (PFA) for 20 min at room temperature (RT) and then permeabilized with 0.5% saponin for 10 min before blocking with PBS + 1% BSA + 5% donkey serum and staining with appropriate antibodies at 1:100 dilution. The following antibodies were used for intracellular cytokine staining from BioLegend: IL-2 (clone JES6-5H3, 503808); TNFα (clone MP6-XT22, 506313), IFN-γ (clone XMG1.2, 505814); IL-17A (clone TC11-18H10.1, 506910, clone BL168, 512310); mouse IgG1 isotype control (clone MOPC-21, 400112, 400135); and mouse IgG2a isotype control (clone MOPC-173, 558055, 558053). For FOXP3 staining, the eBioscience Foxp3 transcription factor buffer set was used (Thermo Fisher Scientific, 00-5523-00) with anti-FOXP3 (clone 150D, BioLegend, 320011). For phosphorylated S6 ribosomal protein (p-S6 Ser240/244) staining, cells were fixed with 4% PFA and then permeabilized with 80% methanol and stained with a p-S6 antibody (clone D68F8, Cell Signaling Technology, 5018S) or isotype control (clone DA1E, Cell Signaling Technology, 2975S).

Confocal microscopy and image analysis

All fluorescence images were imaged with a 100× Plan Apo NA 1.4 objective (Nikon) on a system that includes a Nikon Ti-E chassis, Yokogawa CSU-X1 spinning disk confocal, 405, 488, 561, and 641 nm lasers, motorized Z-axis piezoelectric stage (Applied Scientific), and XR/Mega-10EX camera (Stanford Photonics). The system was controlled by Micro-Manager. We captured 0.2-µm axial slices through the cells. For colocalization, T cells were fixed with 4% PFA, permeabilized with 0.1% Triton X-100 (Sigma-Aldrich, X100), and blocked overnight in PBS plus 5% donkey serum. The cells were stained with primary antibodies anti-YAP1 (Santa Cruz, clone 63.7, sc-101199, and Cell Signaling Technology, clone D8H1X, 14074S) and anti-NFAT1 (Cell Signaling Technology, clone D6W5B, 14793S) sequentially for 1 h at RT, washed, and then counter-stained with donkey anti-mouse, or anti-rabbit secondary antibodies (Jackson ImmunoResearch, 715-605-150, 715-545-151, 711-545-152, 711-605-152). The specimens were covered with Fluoromount G with DAPI (Thermo Fisher Scientific, 00-4959-52) and stored in the dark at 4°C until imaging. Z-stacks were captured with 0.2-µm axial slices as above. Individual T cells were cropped in Fiji and run through a homemade macro in Fiji. Images were subjected to graphical processor unit–based deconvolution (Bruce and Butte, 2013) using a calculated point spread function (Microvolution) and background subtracted in Fiji. For colocalization measurements, we used the Confined Displacement Algorithm implemented in the GDSC Stack Colocalization plugin in Fiji to calculate the Manders coefficient for regions of the images that were selected by the MaxEntropy thresholding method with default parameters (100 permutations, minimum shift 9, maximum shift 16, significance 0.05).

Adoptive transfer mouse models

For adoptive transfer experiments with LCMV infection, naive $SMARTA^+$ $CD4^+$ T cells were isolated from 6–8-wk-old WT or YAPcKO mice (mice are either $CD45.1/2^+$ or $CD45.2^+$). 10^5 cells were adoptively transferred (i.v.) into B6.SJL ($CD45.1^+$) congenic

mice, and then mice were infected with 2 × 10^5 PFU of LCMV Armstrong (i.v.). For adoptive transfer of transduced cells, LCMV was injected 1 d before 5 × 10^5 transduced, 24-h-activated T cells for each condition were transferred into CD45.1$^+$ congenic mice. 5 d after infection, spleens were harvested and cells stained for cell surface markers and intracellular cytokines.

For adoptive transfer experiments with type I diabetes, naive BDC2.5 CD4$^+$ T cells were isolated from 6–8-wk-old BDC2.5 NOD mice and activated on an anti-CD3 (8 µg/ml) coated plate supplemented with anti-CD28 (2 µg/ml) and IL-12 (10 ng/ml). After 24 h, T cells were retrovirally transduced with MSCV-LTRmiR30-PIG (LMP) shRNA vectors (see T cell isolation, activation, proliferation, and retroviral transduction). T cells were taken off anti-CD3 coated plates at 72 h and rested for 48 h in 50 U/ml IL-2. GFP$^+$ cells were sorted, 10^5 T cells were adoptively transferred (i.v.) into NOD.SCID mice, and glucose levels was measured every day using a blood glucose meter. If blood glucose reached over 250 mg/dl for 2 d straight, the mouse was considered diabetic and euthanized.

Extracellular flux and metabolic assays

ECARs and OCRs were measured using a XF96 Extracellular Flux Analyzer (Seahorse Bioscience). For oxidative phosphorylation measurements, cells were washed and resuspended in glucose-free, sodium bicarbonate–free RPMI media + L-glutamine (Sigma-Aldrich, R1383) supplemented with 10 mM glucose (Sigma-Aldrich, G8270), and 1 mM sodium pyruvate (GIBCO BRL, 11360070) and analyzed under basal conditions and following treatment with the following agents: 1 mM oligomycin (Sigma-Aldrich, 75351); 2 mM carbonyl cyanide-4-(trifluoromethoxy)phenylhydrazone (FCCP; Sigma-Aldrich, C2920); 100 nM rotenone (Sigma-Aldrich, R8875), and 1 mM antimycin A (Sigma-Aldrich, A8674). Basal OCR was calculated by subtracting the OCR after rotenone and antimycin A treatment from the OCR before oligomycin treatment. Spare respiratory capacity was calculated by subtracting OCR before oligomycin treatment from OCR before rotenone and antimycin A treatment. Maximal respiratory capacity was calculated by subtracting the OCR after rotenone and antimycin A treatment from the OCR measured after addition of FCCP. For glycolytic measurements, cells were washed and resuspended in glucose-free, sodium bicarbonate–free RPMI media + L-glutamine supplemented with 1 mM sodium pyruvate and analyzed under basal conditions and following treatment with the following agents: 25 mM glucose, 1 mM oligomycin, and 20 mM 2-deoxy-glucose (2-DG; Sigma-Aldrich, D8375). Basal ECAR was calculated by subtracting the ECAR after 2-DG treatment from the ECAR before glucose addition. Glycolysis was calculated by subtracting basal ECAR from ECAR after glucose addition. Maximal glycolytic capacity (MGC) was calculated by subtracting the ECAR after addition of 2-DG from the ECAR measured after addition of oligomycin.

For measuring glucose uptake, T cells were washed with glucose-free RPMI and then incubated with 10 nM 2-NBDG (Thermo Fisher Scientific, N13195) in glucose-free RPMI at 37°C for 20 min, T cells were then washed with T cell media and analyzed for glucose uptake by flow cytometry analysis. For mitochondrial size, T cells were incubated in T cell media with 20 nM MitoTracker Green (Thermo Fisher Scientific, M7514) or 10 nM MitoTracker DeepRed (Thermo Fisher Scientific, M22426) at 37°C for 20 min. Then the T cells were washed and analyzed for MitoTracker staining. For mitochondrial membrane potential, T cells were incubated in T cell media with 20 nM tetramethylrhodamine methyl ester perchlorate (Thermo Fisher Scientific, T668) for 20 min at 37°C and then washed and analyzed for mitochondrial membrane potential. As a positive control, 5 µM FCCP was added to depolarize membrane potential.

Metabolomics and analysis

T cells were purified from spleen and LNs from WT or YAPcKO mice and activated with plate-bound anti-CD3ε (8 µg/ml) in media supplemented with anti-CD28 (2 µg/ml). At 48 h, T cell media were replaced with T cell media containing [U-^{13}C] glucose (Cambridge Isotope Laboratories, CLM-1396-1) or [U-^{13}C] glutamine (Cambridge Isotope Laboratories, CLM-1822-H). At 72 h, T cells were counted and then washed with cold PBS and cold 150 mM ammonium acetate (pH 7.3). To extract intracellular metabolites, 600 µl of cold, 80% methanol was added along with 10 nmol D/L-norvaline (Sigma-Aldrich, N7502-25G), and the mixture was vigorously vortexed while kept on ice. The cellular extracts were clarified by high-speed centrifugation at 4°C, transferred to a glass vial, dried down under vacuum at 30°C, and stored at −80°C.

The samples were analyzed with an UltiMate 3000RSLC HPLC (Thermo Fisher Scientific) coupled to a Q Exactive mass spectrometer (Thermo Fisher Scientific). After resuspension in 50% acetonitrile, 1/10th of each sample was loaded onto a Luna NH2 (3 µm, 100A, 150 mm × 2 mm, Phenomenex) column. Separation was achieved using 5 mM NH_4AcO (pH 9.9) and acetonitrile at a flowrate of 200 µl/min. A gradient from 15% to 90% over 18 min was used, followed by a 9 min isocratic step at 90% and reequilibration to the initial 15% for 7 min. The Q Exactive was run with polarity switching (+3.50 kV/−3.50 kV) in full scan mode with an m/z range of 65–975. Metabolites were quantified with TraceFinder version 3.3 or 4.1 using accurate mass measurements (≤3 ppm) and retention times established with pure standards. Data analysis, including principal component analysis and hierarchical clustering, was performed using UCLA in-house scripts in R. The data were normalized by cell number.

Immunoblotting and coimmunoprecipitation

Cells were lysed in radioimmunoprecipitation assay buffer (Thermo Fisher Scientific, 89900) containing Halt protease inhibitor cocktail (Thermo Fisher Scientific, 78340) and PhosphataseArrest I (Cell Signaling Technology, 5870S). After centrifugation, the soluble fractions of lysates denatured with 4× lithium dodecyl sulfate (LDS) sample buffer (Thermo Fisher Scientific, NP0008) and 10× reducing agent (Thermo Fisher Scientific, B0009). Lysates were then separated by 4–12% Bis-Tris plus gels (Thermo Fisher Scientific, NW04125BOX), and proteins were transferred to nitrocellulose membranes (Thermo Fisher Scientific, IB23002). Membranes were blocked with PBS-Tween containing 5% BSA and probed with the appropriate

primary and infrared fluorophore-conjugated secondary antibodies (Li-Cor Biosciences, 926-32212, 926–32213, 926–68072, 926–68073). The following antibodies were used for immunoblotting. YAP (clone D8H1X, 14074S); NFAT1 (clone D43B1, 5861S); TATA-binding protein (clone D5C9H, 44059S); and DYKDDDDK (FLAG) tag (clone D6W5B, 14793S) were obtained from Cell Signaling Technology. Actin (clone C-4, sc-47778); GAPDH (clone G-9, sc-365062); and IQGAP1 (clone C-9, sc-376021), were obtained from Santa Cruz Biotechnology. Anti-YAP (Y4470) was obtained from Sigma-Aldrich. Anti-NFAT2 (clone 7A6, ab2796) was obtained from Abcam.

For pulldown of proteins associated with IQGAP1 or FLAG-YAP, activated and/or transduced T cells were cross-linked with 2.5–5 mM dithiobis(succinimidyl propionate) (Thermo Fisher Scientific, 22585) for 20 min at RT and quenched with washes in 50 mM Tris, pH 7.6. Cells were lysed with Pierce IP lysis/wash buffer (Thermo Fisher Scientific, 87787) with Halt protease inhibitor cocktail and PhosphataseArrest I. For IQGAP1 pulldown, 500 µg lysate in 300 µl was incubated with either anti-IQGAP1 (Santa Cruz, clone C-9, sc-376021) or mouse IgG (Santa Cruz, sc-2025) overnight at 4°C. Protein G sepharose 4 fast flow (Sigma-Aldrich, GE17-0618-01) was washed in Pierce IP lysis/wash buffer 1×, blocked with PBS + 1% BSA for an hour, and combined with lysates for 2 h at 4°C. The beads were washed in Pierce IP lysis/wash buffer 3× and eluted with 4× LDS sample buffer and 10× reducing agent. For FLAG pulldown, anti-DYKDDDDK affinity resin (clone L5, BioLegend, 651501) was blocked for an hour with PBS + 1% BSA and incubated with 500 µg lysate in 300 µl overnight at 4°C. The beads were washed in Pierce IP lysis/wash buffer 3× and eluted with 4× LDS sample and 10× reducing agent.

For pulldown of proteins associated with IQGAP1 in activated T cells on soft or stiff scaffolds, T cells were cross-linked with 2.5–5 mM dithiobis(succinimidyl propionate) (Thermo Fisher Scientific, 22585) for 20 min at RT and quenched with washes in 50 mM Tris, pH 7.6. Cells were lysed with Pierce IP lysis/wash buffer (Thermo Fisher Scientific, 87787) with Halt protease inhibitor cocktail and PhosphataseArrest I. For IQGAP1 pulldown, 500 µg lysate in 300 µl was incubated with either anti-IQGAP1 (Santa Cruz, clone C-9, sc-376021) or mouse IgG (Santa Cruz, sc-2025) overnight at 4°C. Protein G sepharose 4 fast flow (Sigma-Aldrich, GE17-0618-01) was washed in Pierce IP lysis/wash buffer 1×, blocked with PBS + 1% BSA for an hour, and combined with lysates for 2 h at 4°C. The beads were washed in Pierce IP lysis/wash buffer 3× and eluted with 4× LDS sample buffer and 10× reducing agent. Lysates were then separated by 4–12% Bis-Tris plus gels (Thermo Fisher Scientific, NW04125BOX), and proteins were transferred to nitrocellulose membranes (Thermo Fisher Scientific, IB23002). Membranes were blocked with PBS-Tween containing 5% BSA and probed with the appropriate primary and infrared fluorophore-conjugated secondary antibodies (Li-Cor Biosciences, 926-32212, 926–32213, 926–68072, 926–68073). The following antibodies were used for immunoblotting: YAP (clone D8H1X, 14074S) and NFAT1 (clone D43B1, 5861S) were obtained from Cell Signaling Technology. Actin (clone C-4, sc-47778) and IQGAP1 (clone C-9, sc-376021) were obtained from Santa Cruz Biotechnology.

The following buffers were used for nuclear/cytoplasmic extraction. Cytoplasmic extraction buffer consisted of 10 mM Hepes, 10 mM KCl, 0.1 mM EDTA, and 0.1 mM EGTA in dH_2O with 0.2% NP-40. Nuclear extraction buffer consisted of 20 mM Hepes, 1 mM NaCl, 1 mM EDTA, and 1 mM EGTA in dH_2O with 1% Triton X-100. Added fresh before use of either buffer was 1 mM DTT, 1× Halt protease inhibitor cocktail (Roche) and 1× PhosphataseArrest I. T cells were washed with ice-cold PBS 1×, and then cytoplasmic extraction buffer was added, and the cells were gently resuspended. Cells were incubated on ice for 5 min and then centrifuged for 5 min at 5,000 *g*. The cytoplasmic fraction was removed, and the cell pellet was washed with cytoplasmic extraction buffer 1×. The nuclear extraction buffer was then added and resuspended on ice, with vortexing every 5 min × 15 min. The cells were centrifuged for 20 min at maximum speed, and then the nuclear fraction was collected. A GAPDH antibody was used to assess the purity of the cytoplasmic fraction, and a TATA-binding protein antibody was used to assess the purity of the nuclear fraction.

2D scaffold fabrication

Ultrapure, high-molecular-weight alginate (250 kD; Nova Matrix, 42200106) was first dissolved in deionized water, then purified with activated charcoal, sterile-filtered, frozen, and lyophilized. For peptide modification, the resulting lyophilized ultrapure alginate (1% wt/vol) was then dissolved in 100 nM MES, pH 5.9 (EMD Millipore, 475893) followed by covalent conjugation of RGD peptide (GenScript, RP20297) using carbodiimide chemistry (NHS/EDC) as reported before (Majedi et al., 2018). After an overnight reaction, the solution was dialyzed (molecular weight cutoff, 12 kD) against distilled water for 3 d with decreasing salt concentration. The final solution was then frozen and lyophilized for further use. For the preparation of hydrogels, 1.25 and 2.5% wt/vol alginate solution in PBS was mixed with calcium sulfate slurry (1 M in deionized water) to a final concentration of 10 mM and 40 mM for the soft and stiff formulation, respectively. For homogeneous mixing, two syringes connected with a Luer-lock syringe connector were used. The components were mixed rapidly and cast in cell-culture well plates. For complete gelation, the mixture was allowed to rest 45 min followed by two overnight washes with modified PBS (0.42 mM $CaCl_2$) and T cell media that were supplied by penicillin/streptomycin before addition of cells.

For activating T cells on the 2D hydrogels, C57B/6 splenocytes were first isolated and depleted of T cells using biotin-CD4 and -CD8 antibodies followed by incubation with streptavidin magnetic beads. Then the splenocytes were treated with mitomycin C to prevent cell growth. Splenocytes were pulsed with 100 nM of GP 61–80 peptide and directly mixed with SMARTA TCR transgenic WT or YAPcKO $CD4^+$ T cells at a 3:1 ratio. After 72 h, ∼95% of the living cells were SMARTA T cells. We used Lympholyte M (Cedarlane Labs) to extract the living $CD4^+$ T cells for downstream processing, such as coimmunoprecipitation.

Stiffness measurements of hydrogels and LNs

Mechanical properties of hydrogels were determined in wet state using an Instron Mechanical Apparatus (Instron) under

unconfined compression at a constant speed of 1 mm/min. The elastic modulus E was calculated from the slope of the stress versus strain curves (first 10% of strain). To measure the mechanical properties of LNs after LCMV infection, 6–8-wk C57/B6 mice were infected with 2 × 10^5 PFU of LCMV Armstrong (i.v.). At days 3, 7, 10, and 14, inguinal and brachial LNs were extracted and placed in PBS. LN diameters were measured using a digital caliper. Mechanical properties of extracted LNs were tested by an Instron Mechanical Apparatus (Instron) under unconfined compression at a constant speed of 1 mm/min. The elastic modulus E was calculated as the slope of the stress versus strain curves (first 10% of strain). For rheological assessment of hydrogels, control liver, and PDMS, we used a stress-controlled rheometer (Anton-Paar; MCR 302). Either 8-mm- or 25-mm-diameter soft and hard hydrogels were formed and placed between the instrument's parallel plates bearing roughened surfaces, and a gap of 2 mm was used. Measurements were performed by full amplitude sweeps (10 Hz and 0.01–100% strain) and frequency sweeps (0.01–100 Hz, 0.1% strain) at 37°C. Freshly extracted liver tissue (mouse) and PDMS (1:10) were used as natural and elastic tissue samples, respectively.

RNA isolation and RNA-seq processing and analysis

For activating T cells on the 2D hydrogels, C57B/6 splenocytes congenically marked CD45.1 were first isolated and depleted of T cells using biotin-CD4 and -CD8 antibodies followed by incubation with streptavidin magnetic beads. Then the splenocytes were treated with mitomycin C to prevent cell growth. Splenocytes were pulsed with 100 nM of GP 61–80 peptide and directly mixed with CD45.2 congenic, SMARTA TCR transgenic WT or YAPcKO $CD4^+$ T cells at a 3:1 ratio. After 72 h, we stained for CD4 and CD45.2 and sorted out $CD45.2^+$ $CD4^+$ SMARTA T cells using the Sony SH800S cell sorter for RNA isolation using the Direct-Zol RNA miniprep kit (Zymo Research, R2060). RNA integrity was checked by Agilent Bioanalyzer 2100; only samples with clean ribosomal RNA peaks were used for further experiments.

Library for RNA-Seq was prepared according to KAPA Stranded mRNA-Seq poly(A) selected kit (KAPA Biosystems) using 250 ng total RNAs as input. Final library quality and quantity was analyzed by an Agilent Bioanalyzer 2100 and Life Technologies Qubit3.0 Fluorometer. 150-bp paired-end reads were sequenced on Illumina NovaSeq 6000. The reads were first mapped to the latest University of California Santa Cruz transcript set using Spliced Transcripts to a Reference (STAR) software method (Dobin et al., 2013), and the gene expression level was estimated using RSEM v1.2.15 and DESeq2 (Li and Dewey, 2011). Differentially expressed genes were identified using DESeq2 R package (Love et al., 2014). Genes showing altered expression with adjusted $P < 0.05$ and more than 1.3-fold changes were considered differentially expressed. ClusterProfiler was used to perform the Gene Ontology, Kyoto Encyclopedia of Genes and Genomes, and Reactome enrichment analysis (Yu et al., 2012).

RNA-seq data are available under Gene Expression Omnibus accession no. GSE146643.

Statistical analysis

Permutation testing was used for all statistical comparisons of flow cytometry data, survival curves, fluorescence colocalization, and stiffness. This method reduces the potential influence of outliers and relaxed the requirement of knowing the distribution of observations by comparing the value of the test statistic to a reference distribution generated from the data themselves, rather than to a standard distribution. To ensure that permutation testing was a suitable way to compare means, we showed first that the variances of the two groups were similar by the nonparametric Ansari–Bradley test. We used the permutationTest2 function of the "resample" package of R to calculate two-sided P values and determine the 95% confidence intervals (CIs), performing 50,000–100,000 permutations. All average values in this paper are bootstrapped means, calculated using the "bootstrap" function of the resample package in R. All boxes in figures show the bootstrapped mean and the calculated 95% CI. CIs are calculated using the "CI.t" function of the resample package. Permutation P values are abbreviated in figures by *, $P < 0.05$, **, $P < 0.01$, ***, $P < 0.001$, or directly labeled with the P value itself.

Data and materials availability

There are no restrictions on data availability. Material transfer agreements regulate the sharing of SMARTA and $YAP^{fl/fl}$ mice.

Online supplemental material

Fig. S1 characterizes the engineered hydrogels, shows the nuclear localization of YAP, and reveals the YAP protein expression level in the YAPcKO mouse. Fig. S2 characterizes the YAPcKO mice by flow cytometry, shares transcriptional data from RNA-seq experiments, and shows the early responses of T cells after TCR ligation. Fig. S3 shows the enhanced metabolic flux in YAPcKO T cells and characterizes the amino acid metabolism driven by YAP. Fig. S4 shows the time course of YAP, NFAT1, and IQGAP1 expression and nuclear localization. Fig. S5 offers a schematic of the temporal responses of YAP, and schematic of the interactions of YAP in soft and stiff environments.

Acknowledgments

We thank Fernando Camargo (Boston Children's Hospital, Boston, MA), Calvin Kuo (Stanford University, Stanford, CA), and Shane Crotty (La Jolla Institute, La Jolla, CA) for mice; Jason Cyster (University of California, San Francisco, San Francisco, CA) for LCMV; and the Bollyky laboratory (Stanford University, Stanford, CA) for experimental help. We appreciate suggestions from Profs. Julien Sage and Paul Bollyky.

We acknowledge the Stanford Shared FACS Facility; the UCLA Jonsson Comprehensive Cancer Center Flow Cytometry Core Facility, which is supported by National Institutes of Health awards P30 CA016042 and 5P30 AI028697; and the UCLA Metabolomics core. We acknowledge financial support from the National Institutes of Health (R01 GM110482), the UCLA Jonsson Comprehensive Cancer Center (P30CA016042), the Stanford Child Health Research Institute, and the UCLA Children's Discovery and Innovation Institute.

Author contributions: Conceptualization, analysis, visualization, and writing: K.P. Meng and M.J. Butte; investigation and visualization: K.P. Meng, F.J. Majedi, and T.J. Thauland; resources, funding acquisition, project administration, and supervision: M.J. Butte.

Disclosures: The authors declare no competing interests exist.

Submitted: 12 January 2020
Revised: 10 March 2020
Accepted: 17 March 2020

References

Acton, S.E., A.J. Farrugia, J.L. Astarita, D. Mourão-Sá, R.P. Jenkins, E. Nye, S. Hooper, J. van Blijswijk, N.C. Rogers, K.J. Snelgrove, et al. 2014. Dendritic cells control fibroblastic reticular network tension and lymph node expansion. *Nature*. 514:498–502. https://doi.org/10.1038/nature13814

Alon, R., and M.L. Dustin. 2007. Force as a facilitator of integrin conformational changes during leukocyte arrest on blood vessels and antigen-presenting cells. *Immunity*. 26:17–27. https://doi.org/10.1016/j.immuni.2007.01.002

Astarita, J.L., V. Cremasco, J. Fu, M.C. Darnell, J.R. Peck, J.M. Nieves-Bonilla, K. Song, Y. Kondo, M.C. Woodruff, A. Gogineni, et al. 2015. The CLEC-2-podoplanin axis controls the contractility of fibroblastic reticular cells and lymph node microarchitecture. *Nat. Immunol.* 16:75–84. https://doi.org/10.1038/ni.3035

Bashour, K.T., A. Gondarenko, H. Chen, K. Shen, X. Liu, M. Huse, J.C. Hone, and L.C. Kam. 2014. CD28 and CD3 have complementary roles in T-cell traction forces. *Proc. Natl. Acad. Sci. USA*. 111:2241–2246. https://doi.org/10.1073/pnas.1315606111

Bertero, T., W.M. Oldham, K.A. Cottrill, S. Pisano, R.R. Vanderpool, Q. Yu, J. Zhao, Y. Tai, Y. Tang, Y.Y. Zhang, et al. 2016. Vascular stiffness mechanoactivates YAP/TAZ-dependent glutaminolysis to drive pulmonary hypertension. *J. Clin. Invest.* 126:3313–3335. https://doi.org/10.1172/JCI86387

Bruce, M.A., and M.J. Butte. 2013. Real-time GPU-based 3D Deconvolution. *Opt. Express*. 21:4766–4773. https://doi.org/10.1364/OE.21.004766

Chen, R., S. Bélanger, M.A. Frederick, B. Li, R.J. Johnston, N. Xiao, Y.C. Liu, S. Sharma, B. Peters, A. Rao, et al. 2014. In vivo RNA interference screens identify regulators of antiviral CD4(+) and CD8(+) T cell differentiation. *Immunity*. 41:325–338. https://doi.org/10.1016/j.immuni.2014.08.002

Comrie, W.A., S. Li, S. Boyle, and J.K. Burkhardt. 2015. The dendritic cell cytoskeleton promotes T cell adhesion and activation by constraining ICAM-1 mobility. *J. Cell Biol.* 208:457–473. https://doi.org/10.1083/jcb.201406120

Cox, A.G., K.L. Hwang, K.K. Brown, K. Evason, S. Beltz, A. Tsomides, K. O'Connor, G.G. Galli, D. Yimlamai, S. Chhangawala, et al. 2016. Yap reprograms glutamine metabolism to increase nucleotide biosynthesis and enable liver growth. *Nat. Cell Biol.* 18:886–896. https://doi.org/10.1038/ncb3389

Discher, D.E., P. Janmey, and Y.-L. Wang. 2005. Tissue cells feel and respond to the stiffness of their substrate. *Science*. 310:1139–1143. https://doi.org/10.1126/science.1116995

Dobin, A., C.A. Davis, F. Schlesinger, J. Drenkow, C. Zaleski, S. Jha, P. Batut, M. Chaisson, and T.R. Gingeras. 2013. STAR: ultrafast universal RNA-seq aligner. *Bioinformatics*. 29:15–21. https://doi.org/10.1093/bioinformatics/bts635

Dong, J., G. Feldmann, J. Huang, S. Wu, N. Zhang, S.A. Comerford, M.F. Gayyed, R.A. Anders, A. Maitra, and D. Pan. 2007. Elucidation of a universal size-control mechanism in Drosophila and mammals. *Cell*. 130:1120–1133. https://doi.org/10.1016/j.cell.2007.07.019

Dupont, S., L. Morsut, M. Aragona, E. Enzo, S. Giulitti, M. Cordenonsi, F. Zanconato, J. Le Digabel, M. Forcato, S. Bicciato, et al. 2011. Role of YAP/TAZ in mechanotransduction. *Nature*. 474:179–183. https://doi.org/10.1038/nature10137

Ekberg, H., H. Tedesco-Silva, A. Demirbas, S. Vítko, B. Nashan, A. Gürkan, R. Margreiter, C. Hugo, J.M. Grinyó, U. Frei, et al; ELITE-Symphony Study. 2007. Reduced exposure to calcineurin inhibitors in renal transplantation. *N. Engl. J. Med.* 357:2562–2575. https://doi.org/10.1056/NEJMoa067411

Elosegui-Artola, A., R. Oria, Y. Chen, A. Kosmalska, C. Pérez-González, N. Castro, C. Zhu, X. Trepat, and P. Roca-Cusachs. 2016. Mechanical regulation of a molecular clutch defines force transmission and transduction in response to matrix rigidity. *Nat. Cell Biol.* 18:540–548. https://doi.org/10.1038/ncb3336

Elosegui-Artola, A., I. Andreu, A.E.M. Beedle, A. Lezamiz, M. Uroz, A.J. Kosmalska, R. Oria, J.Z. Kechagia, P. Rico-Lastres, A.-L. Le Roux, et al. 2017. Force Triggers YAP Nuclear Entry by Regulating Transport across Nuclear Pores. *Cell*. 171:1397–1410.e14. https://doi.org/10.1016/j.cell.2017.10.008

Fan, Y., Y. Gao, J. Rao, K. Wang, F. Zhang, and C. Zhang. 2017. YAP-1 Promotes Tregs Differentiation in Hepatocellular Carcinoma by Enhancing TGFBR2 Transcription. *Cell. Physiol. Biochem.* 41:1189–1198. https://doi.org/10.1159/000464380

Gorman, J.A., A. Babich, C.J. Dick, R.A. Schoon, A. Koenig, T.S. Gomez, J.K. Burkhardt, and D.D. Billadeau. 2012. The cytoskeletal adaptor protein IQGAP1 regulates TCR-mediated signaling and filamentous actin dynamics. *J. Immunol.* 188:6135–6144. https://doi.org/10.4049/jimmunol.1103487

Hu, K.H., and M.J. Butte. 2016. T cell activation requires force generation. *J. Cell Biol.* 213:535–542. https://doi.org/10.1083/jcb.201511053

Judokusumo, E., E. Tabdanov, S. Kumari, M.L. Dustin, and L.C. Kam. 2012. Mechanosensing in T lymphocyte activation. *Biophys. J.* 102:L5–L7. https://doi.org/10.1016/j.bpj.2011.12.011

Kim, S.T., K. Takeuchi, Z.-Y.J. Sun, M. Touma, C.E. Castro, A. Fahmy, M.J. Lang, G. Wagner, and E.L. Reinherz. 2009. The alphabeta T cell receptor is an anisotropic mechanosensor. *J. Biol. Chem.* 284:31028–31037. https://doi.org/10.1074/jbc.M109.052712

Klein-Hessling, S., K. Muhammad, M. Klein, T. Pusch, R. Rudolf, J. Flöter, M. Qureischi, A. Beilhack, M. Vaeth, C. Kummerow, et al. 2017. NFATc1 controls the cytotoxicity of CD8$^+$ T cells. *Nat. Commun.* 8:511. https://doi.org/10.1038/s41467-017-00612-6

Koo, J.H., and K.L. Guan. 2018. Interplay between YAP/TAZ and Metabolism. *Cell Metab.* 28:196–206. https://doi.org/10.1016/j.cmet.2018.07.010

Lamar, J.M., P. Stern, H. Liu, J.W. Schindler, Z.G. Jiang, and R.O. Hynes. 2012. The Hippo pathway target, YAP, promotes metastasis through its TEAD-interaction domain. *Proc. Natl. Acad. Sci. USA*. 109:E2441–E2450. https://doi.org/10.1073/pnas.1212021109

Li, B., and C.N. Dewey. 2011. RSEM: accurate transcript quantification from RNA-Seq data with or without a reference genome. *BMC Bioinformatics*. 12:323. https://doi.org/10.1186/1471-2105-12-323

Li, Z., H. Lee, and C. Zhu. 2016. Molecular mechanisms of mechanotransduction in integrin-mediated cell-matrix adhesion. *Exp. Cell Res.* 349:85–94. https://doi.org/10.1016/j.yexcr.2016.10.001

Lian, I., J. Kim, H. Okazawa, J. Zhao, B. Zhao, J. Yu, A. Chinnaiyan, M.A. Israel, L.S.B. Goldstein, R. Abujarour, et al. 2010. The role of YAP transcription coactivator in regulating stem cell self-renewal and differentiation. *Genes Dev.* 24:1106–1118. https://doi.org/10.1101/gad.1903310

Lian, J., M. Cuk, S. Kahlfuss, L. Kozhaya, M. Vaeth, F. Rieux-Laucat, C. Picard, M.J. Benson, A. Jakovcevic, K. Bilic, et al. 2017. ORAI1 mutations abolishing store-operated Ca2+entry cause anhidrotic ectodermal dysplasia with immunodeficiency. *J. Allergy Clin. Immunol.* https://doi.org/10.1016/j.jaci.2017.10.031

Liu, B., W. Chen, B.D. Evavold, and C. Zhu. 2014. Accumulation of dynamic catch bonds between TCR and agonist peptide-MHC triggers T cell signaling. *Cell*. 157:357–368. https://doi.org/10.1016/j.cell.2014.02.053

Liu, Y., L. Blanchfield, V.P.-Y. Ma, R. Andargachew, K. Galior, Z. Liu, B. Evavold, and K. Salaita. 2016. DNA-based nanoparticle tension sensors reveal that T-cell receptors transmit defined pN forces to their antigens for enhanced fidelity. *Proc. Natl. Acad. Sci. USA*. 113:5610–5615. https://doi.org/10.1073/pnas.1600163113

Love, M.I., W. Huber, and S. Anders. 2014. Moderated estimation of fold change and dispersion for RNA-seq data with DESeq2. *Genome Biol.* 15:550. https://doi.org/10.1186/s13059-014-0550-8

Ma, E.H., G. Bantug, T. Griss, S. Condotta, R.M. Johnson, B. Samborska, N. Mainolfi, V. Suri, H. Guak, M.L. Balmer, et al. 2017. Serine Is an Essential Metabolite for Effector T Cell Expansion. *Cell Metab.* 25:345–357. https://doi.org/10.1016/j.cmet.2016.12.011

Majedi, F.S., M.M. Hasani-Sadrabadi, Y. Kidani, T.J. Thauland, A. Moshaverinia, M.J. Butte, S.J. Bensinger, and L.-S. Bouchard. 2018. Cytokine Secreting Microparticles Engineer the Fate and the Effector Functions of T-Cells. *Adv. Mater.* 30. 1703178. https://doi.org/10.1002/adma.201703178

Mak, T.W., M. Grusdat, G.S. Duncan, C. Dostert, Y. Nonnenmacher, M. Cox, C. Binsfeld, Z. Hao, A. Brüstle, M. Itsumi, et al. 2017. Glutathione Primes

T Cell Metabolism for Inflammation. *Immunity*. 46:675–689. https://doi.org/10.1016/j.immuni.2017.03.019

Martinez, G.J., R.M. Pereira, T. Äijö, E.Y. Kim, F. Marangoni, M.E. Pipkin, S. Togher, V. Heissmeyer, Y.C. Zhang, S. Crotty, et al. 2015. The transcription factor NFAT promotes exhaustion of activated CD8+ T cells. *Immunity*. 42:265–278. https://doi.org/10.1016/j.immuni.2015.01.006

Misra, J.R., and K.D. Irvine. 2018. The Hippo Signaling Network and Its Biological Functions. *Annu. Rev. Genet*. 52:65–87. https://doi.org/10.1146/annurev-genet-120417-031621

Mo, J.-S.. 2017. The role of extracellular biophysical cues in modulating the Hippo-YAP pathway. *BMB Rep*. 50:71–78. https://doi.org/10.5483/BMBRep.2017.50.2.199

Ni, X., J. Tao, J. Barbi, Q. Chen, B.V. Park, Z. Li, N. Zhang, A. Lebid, A. Ramaswamy, P. Wei, et al. 2018. YAP is essential for treg-mediated suppression of antitumor immunity. *Cancer Discov*. 8:1026–1043. https://doi.org/10.1158/2159-8290.CD-17-1124

Peng, C., Y. Zhu, W. Zhang, Q. Liao, Y. Chen, X. Zhao, Q. Guo, P. Shen, B. Zhen, X. Qian, et al. 2017. Regulation of the Hippo-YAP Pathway by Glucose Sensor O-GlcNAcylation. *Mol. Cell*. 68:591–604.e5. https://doi.org/10.1016/j.molcel.2017.10.010

Ron-Harel, N., J.M. Ghergurovich, G. Notarangelo, M.W. LaFleur, Y. Tsubosaka, A.H. Sharpe, J.D. Rabinowitz, and M.C. Haigis. 2019. T Cell Activation Depends on Extracellular Alanine. *Cell Rep*. 28:3011–3021.e4. https://doi.org/10.1016/j.celrep.2019.08.034

Roy, N.H., and J.K. Burkhardt. 2018. The Actin Cytoskeleton: A Mechanical Intermediate for Signal Integration at the Immunological Synapse. *Front. Cell Dev. Biol*. 6:116. https://doi.org/10.3389/fcell.2018.00116

Saitakis, M., S. Dogniaux, C. Goudot, N. Bufi, S. Asnacios, M. Maurin, C. Randriamampita, A. Asnacios, and C. Hivroz. 2017. Different TCR-induced T lymphocyte responses are potentiated by stiffness with variable sensitivity. *eLife*. 6. e23190. https://doi.org/10.7554/eLife.23190

Sayedyahossein, S., Z. Li, A.C. Hedman, C.J. Morgan, and D.B. Sacks. 2016. IQGAP1 Binds to Yes-associated Protein (YAP) and Modulates Its Transcriptional Activity. *J. Biol. Chem*. 291:19261–19273. https://doi.org/10.1074/jbc.M116.732529

Sharma, S., G.M. Findlay, H.S. Bandukwala, S. Oberdoerffer, B. Baust, Z. Li, V. Schmidt, P.G. Hogan, D.B. Sacks, and A. Rao. 2011. Dephosphorylation of the nuclear factor of activated T cells (NFAT) transcription factor is regulated by an RNA-protein scaffold complex. *Proc. Natl. Acad. Sci. USA*. 108:11381–11386. https://doi.org/10.1073/pnas.1019711108

Sinclair, L.V., J. Rolf, E. Emslie, Y.-B. Shi, P.M. Taylor, and D.A. Cantrell. 2013. Control of amino-acid transport by antigen receptors coordinates the metabolic reprogramming essential for T cell differentiation. *Nat. Immunol*. 14:500–508. https://doi.org/10.1038/ni.2556

Sukumar, M., J. Liu, G.U. Mehta, S.J. Patel, R. Roychoudhuri, J.G. Crompton, C.A. Klebanoff, Y. Ji, P. Li, Z. Yu, et al. 2016. Mitochondrial Membrane Potential Identifies Cells with Enhanced Stemness for Cellular Therapy. *Cell Metab*. 23:63–76. https://doi.org/10.1016/j.cmet.2015.11.002

Thaventhiran, J.E.D., A. Hoffmann, L. Magiera, M. de la Roche, H. Lingel, M. Brunner-Weinzierl, and D.T. Fearon. 2012. Activation of the Hippo pathway by CTLA-4 regulates the expression of Blimp-1 in the CD8+ T cell. *Proc. Natl. Acad. Sci. USA*. 109:E2223–E2229. https://doi.org/10.1073/pnas.1209115109

Totaro, A., T. Panciera, and S. Piccolo. 2018. YAP/TAZ upstream signals and downstream responses. *Nat. Cell Biol*. 20:888–899. https://doi.org/10.1038/s41556-018-0142-z

Vaeth, M., M. Maus, S. Klein-Hessling, E. Freinkman, J. Yang, M. Eckstein, S. Cameron, S.E. Turvey, E. Serfling, F. Berberich-Siebelt, et al. 2017. Store-Operated Ca^{2+} Entry Controls Clonal Expansion of T Cells through Metabolic Reprogramming. *Immunity*. 47:664–679.e6. https://doi.org/10.1016/j.immuni.2017.09.003

Wang, S., F. Xie, F. Chu, Z. Zhang, B. Yang, T. Dai, L. Gao, L. Wang, L. Ling, J. Jia, et al. 2017. YAP antagonizes innate antiviral immunity and is targeted for lysosomal degradation through IKKε-mediated phosphorylation. *Nat. Immunol*. 18:733–743. https://doi.org/10.1038/ni.3744

Willingham, A.T., A.P. Orth, S. Batalov, E.C. Peters, B.G. Wen, P. Aza-Blanc, J.B. Hogenesch, and P.G. Schultz. 2005. A strategy for probing the function of noncoding RNAs finds a repressor of NFAT. *Science*. 309:1570–1573. https://doi.org/10.1126/science.1115901

van der Windt, G.J.W., D. O'Sullivan, B. Everts, S.C. Huang, M.D. Buck, J.D. Curtis, C.H. Chang, A.M. Smith, T. Ai, B. Faubert, et al. 2013. CD8 memory T cells have a bioenergetic advantage that underlies their rapid recall ability. *Proc. Natl. Acad. Sci. USA*. 110:14336–14341. https://doi.org/10.1073/pnas.1221740110

You, S., C. Chen, W.-H. Lee, C.-H. Wu, V. Judkowski, C. Pinilla, D.B. Wilson, and C.-P. Liu. 2003. Detection and characterization of T cells specific for BDC2.5 T cell-stimulating peptides. *J. Immunol*. 170:4011–4020. https://doi.org/10.4049/jimmunol.170.8.4011

Yu, G., L.-G. Wang, Y. Han, and Q.-Y. He. 2012. clusterProfiler: an R package for comparing biological themes among gene clusters. *OMICS*. 16:284–287. https://doi.org/10.1089/omi.2011.0118

Zhao, B., X. Ye, J. Yu, L. Li, W. Li, S. Li, J. Yu, J.D. Lin, C.-Y. Wang, A.M. Chinnaiyan, et al. 2008. TEAD mediates YAP-dependent gene induction and growth control. *Genes Dev*. 22:1962–1971. https://doi.org/10.1101/gad.1664408

Zhao, B., L. Li, K. Tumaneng, C.-Y. Wang, and K.-L. Guan. 2010. A coordinated phosphorylation by Lats and CK1 regulates YAP stability through SCF(beta-TRCP). *Genes Dev*. 24:72–85. https://doi.org/10.1101/gad.1843810

Supplemental material

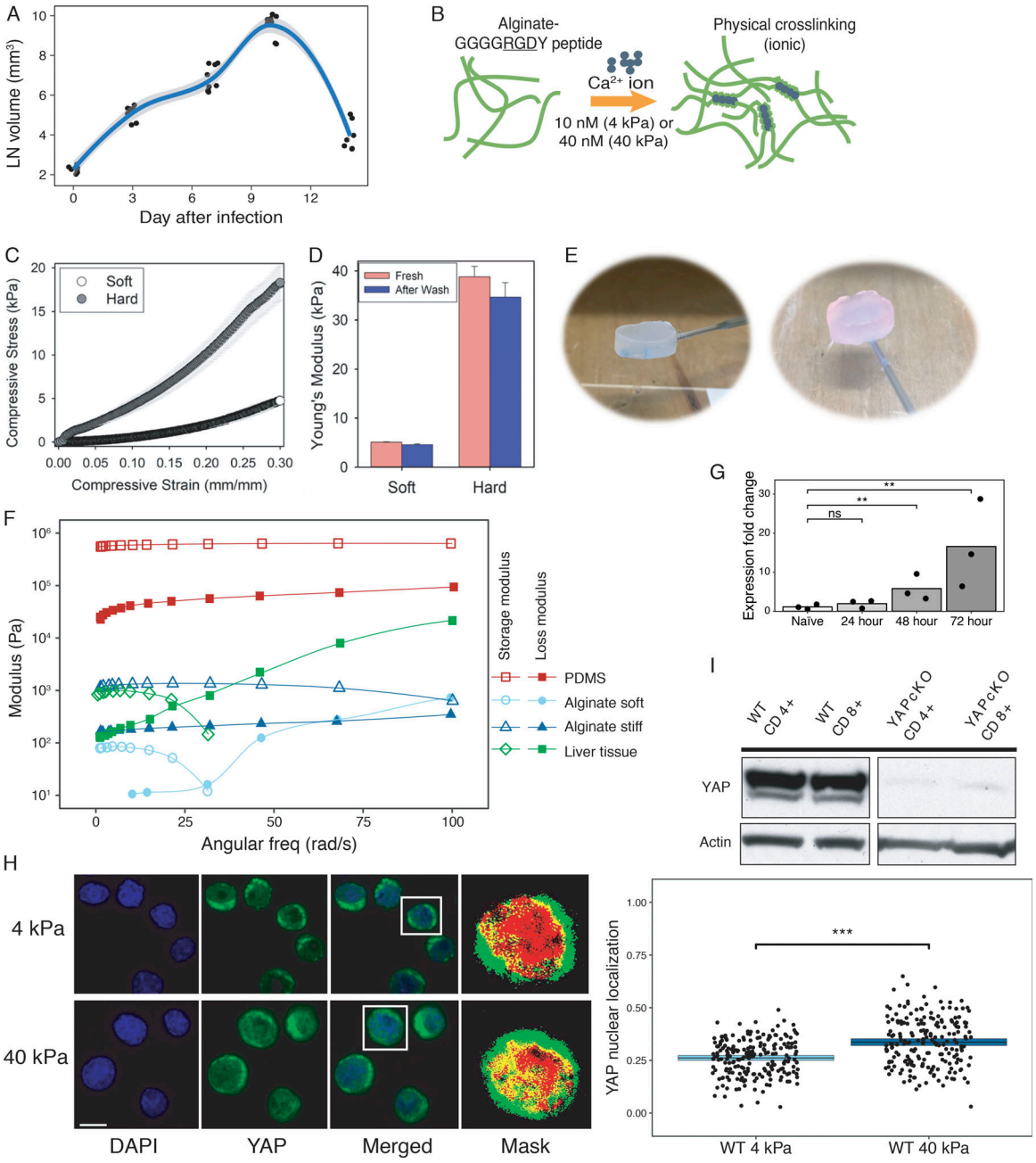

Figure S1. **Characterization of engineered alginate-RGD hydrogels. (A)** Inguinal and brachial LNs from LCMV-infected mice measured for size. Each point represents one LN. Two or three LNs were measured from each mouse × three mice at each time point. Data representative of three independent experiments. **(B)** Schematic of alginate-RGD hydrogels ionically cross-linked with calcium. **(C)** Compressive stress/strain measured for alginate-RGD matrices. **(D)** Young's modulus of matrices before and after washing with PBS to soak excess calcium and equilibrated with T cell media. **(E)** Images of matrices before and after washes with T cell media. **(F)** Rheology measurements to quantify stress relaxation of 2D polydimethylsiloxane (PDMS), 2D alginate hydrogels, and liver tissue with a compressional strain of 1%. Shear storage and loss modulus are displayed over time. **(G)** RNA transcription of YAP by quantitative RT-PCR normalized to actin within each experiment and then to the average of naive. Each dot shows one independent experiment. **(H)** Representative immunofluorescence images show YAP localization in WT CD4$^+$ T cells on soft or stiff alginate scaffolds. Scale bar, 5 µm. The percentage of YAP in the nucleus was analyzed by colocalization analysis. Each point represents a single T cell, $n > 200$ per condition. Data representative of three independent experiments. Box shows mean and 95% CI. **(I)** Immunoblot for YAP in activated CD4$^+$ and CD8$^+$ T cells in 6–8-wk-old YAP$^{fl/fl}$ (WT) or YAP$^{fl/fl}$ × CD4-cre (YAPcKO) mice. Data representative of two independent experiments. Box shows mean and 95% CI. Permutation P values: *, $P < 0.05$; **, $P < 0.01$; ***, $P < 0.001$; ns, not significant.

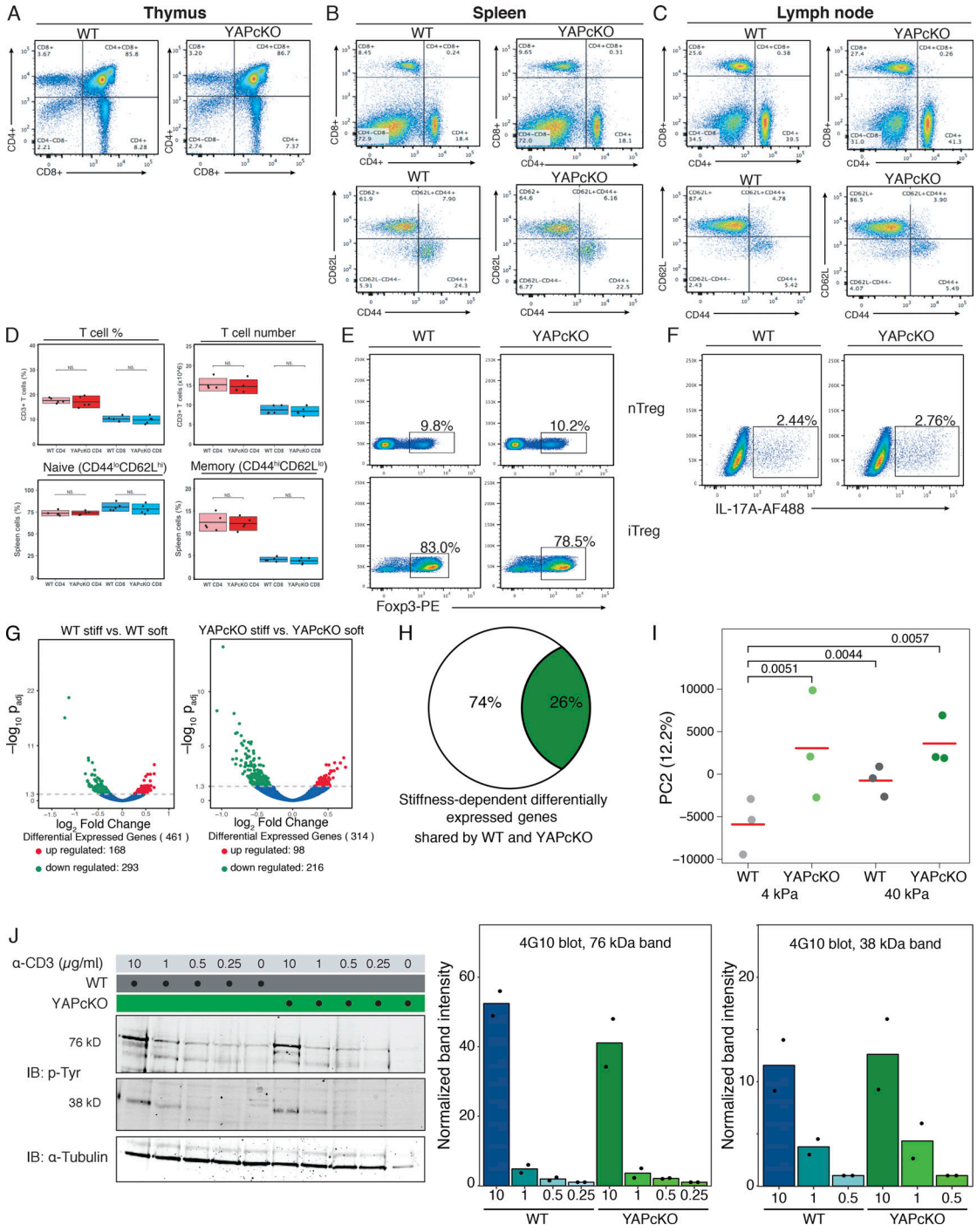

Figure S2. **Characterization of T cells in WT versus YAPcKO mice. (A)** Flow-cytometric analysis of thymocytes from WT and YAPcKO mice. Data representative of four independent experiments. **(B)** Flow-cytometric analysis of splenocytes in WT and YAPcKO mice. Data representative of five independent experiments. **(C)** Flow-cytometric analysis of LNs in WT and YAPcKO mice. Data representative of four independent experiments. **(D)** Naive ($CD62L^{high}CD44^{low}$), and memory phenotype ($CD62L^{low}CD44^{high}$) T cells in the spleen in WT and YAPcKO mice. Data from five independent experiments are shown. Box shows mean and 95% CI. **(E)** Measurement of Foxp3 expression in $CD4^+$ T cells taken ex vivo from splenocytes of WT and YAPcKO mice (natural T reg cells; nTreg); and of Foxp3 expression in $CD4^+$ WT and YAPcKO T cells activated with CD3/CD28 and treated with TGF-β (2 ng/ml) for 3 d (induced T reg cells; iTreg). Data representative of three independent experiments. **(F)** Intracellular cytokine staining for IL-17A in Th17-skewed WT and YAPcKO T cells 4 d after activation. Data representative of three independent experiments. **(G)** Volcano plots of differentially expressed genes (DEG) in WT T cells or YAPcKO T cells cultured with peptide and WT APCs on stiff versus soft substrates. **(H)** Pie graph indicates stiffness-dependent DEG that were identified in only WT T cells (74%) and stiffness-dependent DEG that were identified in both WT and YAPcKO T cells experiencing mechanical stiffness (green, 26%). **(I)** Differentially expressed genes plotted against the second principal component, which accounts for 12.2% of the variance, shows WT cells experiencing a stiff environment were separated from all other groups (permuted P values shown). All other pairwise comparisons were not significant. Bootstrap mean shown as horizontal bar. **(J)** Immunoblot for tyrosine phosphorylation of proximal TCR signaling proteins in acutely activated WT or YAPcKO T cells. 76 kD and 38 kD represent SLP-76 and LAT proteins.

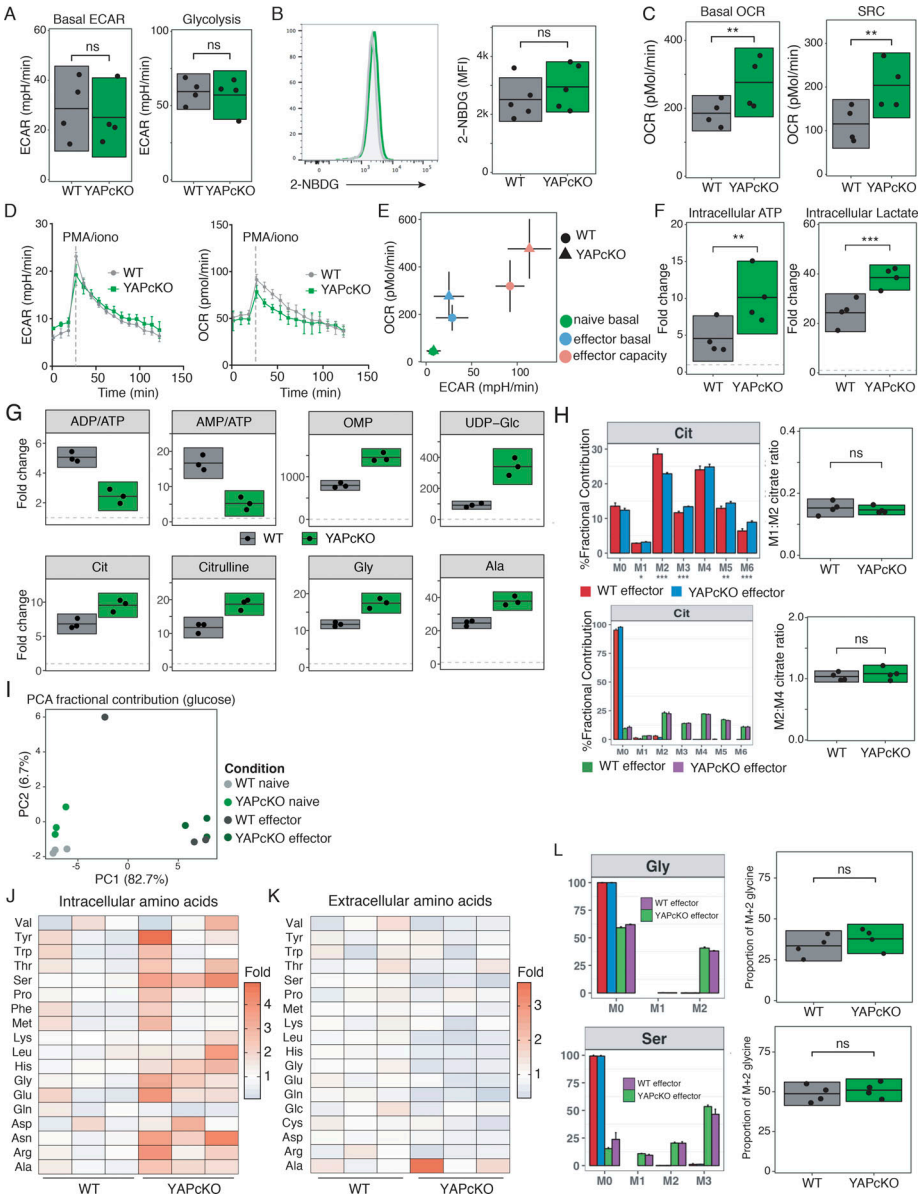

Figure S3. **YAPcKO T cells exhibit greater metabolic flux and amino acid metabolism. (A)** ECAR of WT (gray) and YAPcKO (green) day 3 effector T cells measured under basal conditions and in response to glucose, oligomycin, and 2-DG. Data from four independent experiments are shown. Box shows mean and 95% CI. **(B)** Glucose uptake by 2-NBDG staining in effector WT and YAPcKO T cells. Data from five independent experiments are shown. Box shows mean and 95% CI. **(C)** OCR of WT and YAPcKO day 3 effector T cells was measured in real time under basal conditions and in response to oligomycin, FCCP, and rotenone/antimycin A. Data from four independent experiments are shown. Box shows mean and 95% CI. **(D)** Extracellular flux assay of WT and YAPcKO T cells stimulated with PMA/ionomycin (iono). Data representative of two independent experiments. **(E)** Basal ECAR and OCR values from naive and effector WT and YAPcKO T cells and MGC and maximal respiratory capacity from effector WT and YAPcKO T cells were plotted. Points and whiskers shown represent the mean and 95% CI for four independent experiments. **(F)** Fold change of intracellular ATP or lactate between effector WT and YAPcKO T cells normalized to naive WT or YAPcKO T cell levels (gray dotted line), respectively. Data from four independent experiments shown. Box shows mean and 95% CI. **(G)** Metabolites that comprise the principal component that separates WT and YAPcKO effector T cells. Data representative of three independent experiments. Each point represents a technical replicate. Box shows mean and 95% CI. OMP, orotidine 5′-monophosphate; UDP, uridine diphosphate. **(H)** 13C-glucose labeling and ^{13}C-glutamine labeling of citrate (Cit) isotopomers in effector WT and YAPcKO T cells. Bar graph shows one representative plot of four independent experiments. Each point is an independent experiment. Box shows mean and 95% CI. **(I)** Principal component analysis of fractional contribution of polar metabolites in naive and effector WT and YAPcKO T cells. Data show three independent experiments. **(J)** Heatmap of intracellular amino acid abundance in effector WT and YAPcKO T cells. Intracellular amino acid abundance in WT or YAPcKO effector T cells were first normalized to their respective naive counterparts. Data are shown as fold change of WT or YAPcKO T effector cells normalized to the average amino acid abundance from WT T cells. Data from three independent experiments are shown. **(K)** Heatmap of extracellular amino acid abundance in effector WT and YAPcKO T cells. Extracellular amino acid abundance in WT or YAPcKO effector T cells was first normalized to their respective naive counterparts. Data are shown as a fold change of WT or YAPcKO effector cells normalized to the average metabolite abundance in the media of WT T cells. Data from three independent experiments are shown. **(L)** ^{13}C-glucose contribution to serine m+3 and glycine m+2 in naive and effector WT and YAPcKO T cells. Bar graph shows one representative plot of four independent experiments. Data from four independent experiments are shown. Box shows mean and 95% CI. Permutation P values: *, P < 0.05; **, P < 0.01; ***, P < 0.001; ns, not significant.

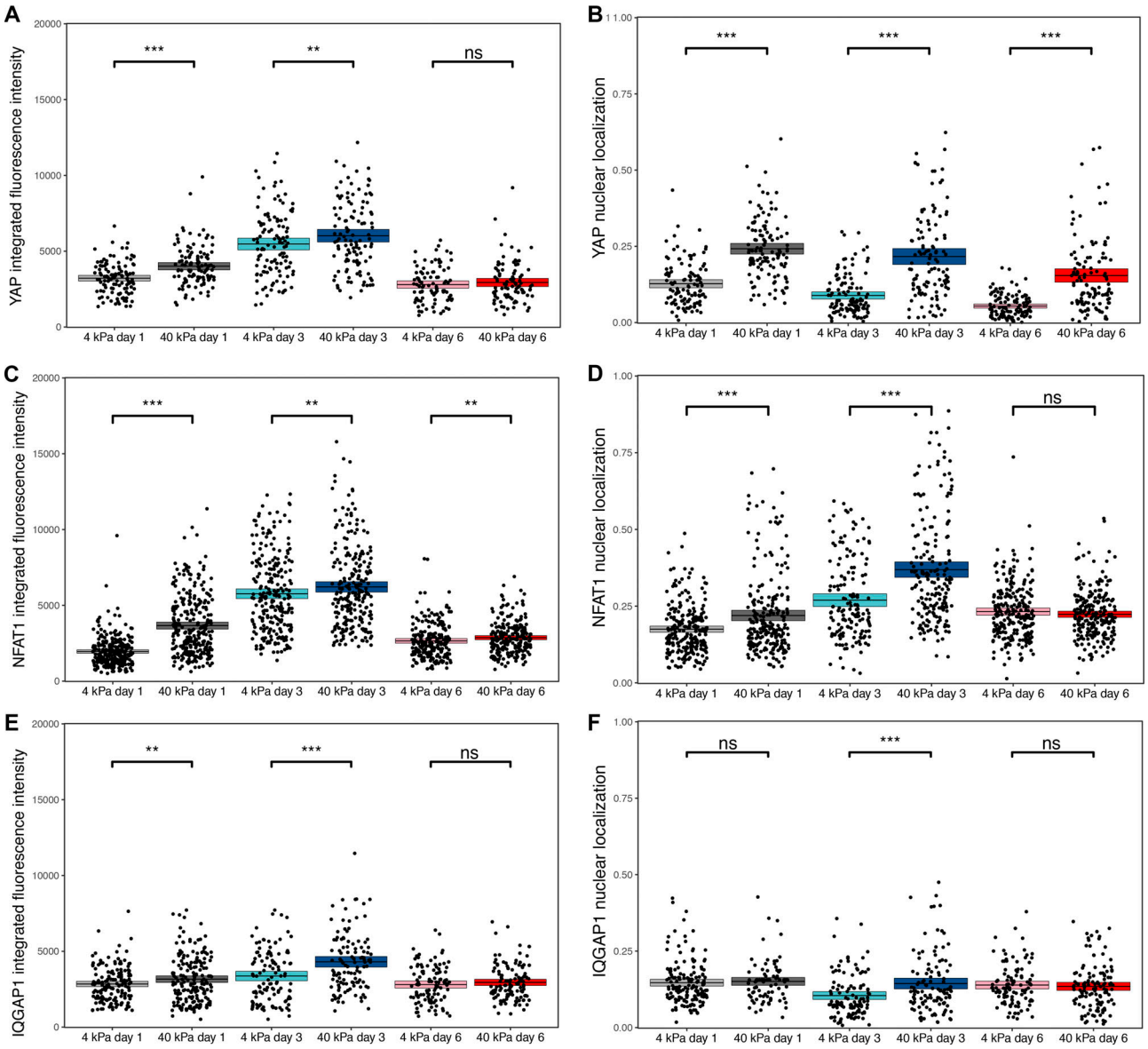

Figure S4. **Time course of YAP, NFAT1, and IQGAP1 expression and nuclear localization. (A–F)** Time course of expression (A, C, and E) and nuclear localization (B, D, and F) of YAP (A and B), NFAT1 (C and D), and IQGAP1 (E and F) dependent on the mechanical microenvironment (soft, 4 kPa; stiff, 40 kPa). Integrated fluorescence intensity across the z-stack of each cell corresponds to the per-cell expression of that protein. Nuclear localization is quantified by fluorescence colocalization with DAPI. Each dot is a single T cell, and box shows bootstrapped mean and 95% CI.

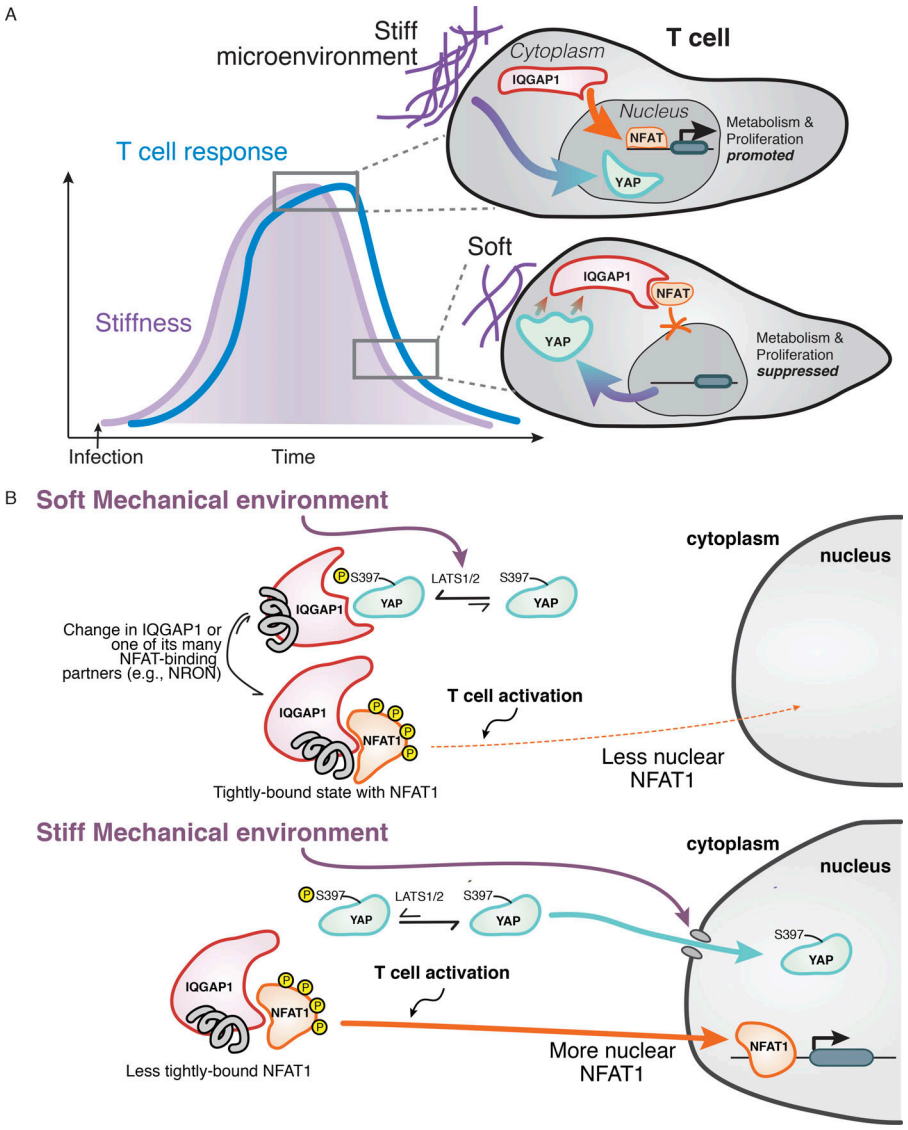

Figure S5. **Microenvironmental mechanoregulation of T cells by YAP. (A)** Schematic depicting how the mechanical microenvironment of tissues regulates T cell activation and metabolism through YAP. In tissues with a soft extracellular matrix microenvironment, such as after an infection resolves or in bystander tissues, YAP localizes in the cytoplasm and interacts with IQGAP1 directly, which sequesters NFAT1 from the nucleus. **(B)** Schematic model of YAP regulation. In a soft microenvironment, YAP bearing S397 interacts with IQGAP1 (red) and its complex of associated proteins that bind NFAT (gray squiggle). In a soft environment, NFAT1 (orange) is preferentially sequestered in the cytoplasm in complex with IQGAP1 in a YAP-dependent manner. In stiff microenvironments, YAP is preferentially localized in the nucleus and does not interact with IQGAP1, which is exclusively cytoplasmic, allowing more facile localization of NFAT1 to the nucleus upon T cell activation.